

Highlights

Design of low-energy transfers in cislunar space using sequences of lobe dynamics

Naoki Hiraiwa, Mai Bando, Yuzuru Sato, Shinji Hokamoto

- A new low-energy trajectory design method based on lobe dynamics is proposed.
- The proposed method systematically combines the sequences of multiple lobe dynamics.
- The application to the fuel-optimal Earth–Moon transfer is demonstrated.

Design of low-energy transfers in cislunar space using sequences of lobe dynamics

Naoki Hiraiwa^{a,*}, Mai Bando^a, Yuzuru Sato^b, Shinji Hokamoto^a

^a*Department of Aeronautics and Astronautics, Kyushu University, 744 Motooka,
Nishu-ku, Fukuoka, 819-0395, Fukuoka, Japan*

^b*RIES-MSC / Department of Mathematics, Hokkaido University, N12 W7
Kita-ku, Sapporo, 060-0812, Hokkaido, Japan*

Abstract

Dynamical structures in the circular restricted three-body problem (CR3BP) are fundamental for designing low-energy transfers, as they aid in analyzing phase space transport and designing desirable trajectories. This study focuses on lobe dynamics to exploit local chaotic transport around celestial bodies, and proposes a new method for systematically designing low-energy transfers by combining multiple lobe dynamics. A graph-based framework is constructed to explore possible transfer paths between departure and arrival orbits, reducing the complexity of the combinatorial optimization problem for designing fuel-efficient transfers. Based on this graph, low-energy transfer trajectories are constructed by connecting chaotic orbits within lobes. The resulting optimal trajectory in the Earth–Moon CR3BP is then converted into an optimal transfer in the bicircular restricted four-body problem using multiple shooting. The obtained transfer is compared with existing optimal solutions to demonstrate the effectiveness of the proposed method.

Keywords: Low-energy transfer, Lobe dynamics, Effective lobes, Circular restricted three-body problem, Bicircular restricted four-body problem

^{*}Corresponding author

Email addresses: hiraiwa.naoki.978@gmail.com (Naoki Hiraiwa),
mbando@aero.kyushu-u.ac.jp (Mai Bando), ysato@math.sci.hokudai.ac.jp (Yuzuru Sato), hokamoto@aero.kyushu-u.ac.jp (Shinji Hokamoto)

1. Introduction

Space exploration in cislunar space has attracted increasing interest due to the Artemis program [1] and the growing number of small satellite missions [2, 3]. Cislunar missions have different requirements for fuel consumption and time of flight, which directly affect trajectory design. Recent missions such as Chang'e-3 [4, 5], Artemis 1 [6, 7], and Chandrayaan-3 [8] used fast transfer trajectories that require more fuel. In contrast, missions like Hiten [9, 10], SMART-1 [11, 12], GRAIL [13], CAPSTONE [14], and SLIM [15–17] adopted fuel-efficient transfers with longer time of flight. A key challenge in trajectory design is to find a variety of transfer options that meet specific mission criteria [18]. This is difficult because multi-body environments like cislunar space are highly sensitive to initial conditions, with spacecraft influenced by multiple celestial bodies simultaneously. Trajectory design in such environments must harness the chaotic dynamics [19, 20].

Trajectory design methods in literature fall into two main categories: numerical and geometrical. Numerical approaches (e.g., Refs. [21–24]) identify transfer trajectories by solving optimization problems. By evaluating a large set of initial conditions, these methods can find a wide range of solutions for fuel consumption and time of flight, often yielding Pareto-optimal sets. Their drawbacks include the need for accurate initial guesses and high computational cost. Geometrical or dynamical systems approaches (e.g., Refs. [25–31]) use the natural dynamics described by dynamical systems theory to generate low-energy transfers. These approaches are limited to planar problems and often result in longer transfer times. The Genesis mission [32, 33] was the first to demonstrate the practical value of this approach by designing its nominal trajectory using modern dynamical systems theory. Both approaches are valuable and complementary, but further development of the geometrical approach is crucial to address the key challenge in trajectory design. The geometrical approach identifies desirable trajectories by analyzing phase space transport, while the numerical approach focuses on local dynamics near given points. Although the numerical approach may imply underlying dynamical structures, the geometrical approach is generally more effective at providing a variety of trajectories with specific properties.

The geometrical approach produces low-energy transfers based on chaotic transport in natural flows, as described by the theories of lobe dynamics and tube dynamics (e.g., Refs. [34–36]). These theories utilize invariant manifolds associated with periodic orbits in the planar circular restricted three-body

problem (CR3BP) [37]. The four-dimensional phase space in the planar CR3BP is often analyzed using a two-dimensional Poincaré map. If periodic orbits appear as points on a Poincaré map, their manifolds may reveal lobe dynamics; otherwise, the manifolds may describe tube dynamics. Thus, it is important to analyze the manifolds of periodic orbits with an appropriate Poincaré map.

Tube dynamics [25, 38] describes global transport between two celestial bodies based on the stable and unstable manifolds of libration point orbits [34], especially around L_1 or L_2 in the planar CR3BP. These manifolds are called *Conley–McGehee tubes* or simply *tubes* [38]. The tubes around L_1 and L_2 provide a framework for understanding the dynamics in the planar CR3BP, as shown in Ref. [26]. For example, the natural orbit transitions of Jupiter comets are described using tube dynamics in the Sun–Jupiter system [39]. Tube dynamics also explains the mechanism of ballistic lunar transfers through Earth–Moon L_2 , enabling systematic design of such transfers [40]. One limitation of tube dynamics is that tubes associated with L_1 Lyapunov orbits do not help depart from the primary, as they move away from it in the CR3BP. Another limitation is the difficulty of applying this method to interplanetary transfers in the Solar System [36]. For example, tubes in the Sun–Earth and Sun–Mars planar CR3BP do not naturally intersect [36, 41].

Lobe dynamics describes finer transport between regions around a single celestial body [34]. This theory was first developed to analyze fluid mixing in two-dimensional inviscid incompressible flows [42] and then extended to two-dimensional, area- and orientation-preserving maps [43]. In such maps, segments of the stable and unstable manifolds associated with periodic points may form small enclosed regions called *lobes*, which are key to transport by lobe dynamics. Within the theory of transport in dynamical systems [44, 45], this idea has been used to analyze the chaotic transport of phase space volume between regions in various fields, such as fluid dynamics [46–50], geophysical flows [51–53], celestial mechanics [36, 54], and chemical reaction dynamics [55, 56]. Computational tools for lobe area and transport rate [57, 58] have been developed, since applying lobe dynamics is limited by the computational difficulty of numerically identifying lobes [34]. In spacecraft trajectory design, lobe dynamics typically leverages the stable and unstable manifolds of resonant orbits. Previous studies [59, 60] have developed trajectory design methods that use multiple gravity assists of Jupiter’s moons by numerically exploiting lobe dynamics in the Jovian system. Further, Refs. [61, 62] have

used the lobe dynamics of the 3:1 resonant orbit to design transfers to the Moon in the Earth–Moon system. In summary, lobe dynamics has been numerically investigated for moon-to-moon transfers or analytically applied around a single resonant orbit for trajectory design in the literature. These studies have yet to provide a simple interpretation of phase space transport for trajectory design based on lobe dynamics.

Unlike the previous studies [59–62], this study proposes a new method that systematically incorporates the dynamical structures of lobes associated with multiple resonant orbits into trajectory design. Earlier work by the authors’ group [30] provided the first theoretical investigation into the combination of multiple lobe dynamics in the standard map [63] via a graph-based framework. That Letter [30] also included a preliminary application to the planar CR3BP. This paper fully develops and validates a trajectory design method based on this approach. The proposed method is applied to construct Earth–Moon transfers in both the CR3BP and the bicircular restricted four-body problem (BCR4BP) [64, 65]. Numerical results demonstrate that lobe dynamics can reveal connections between a celestial body and a tube, which is difficult to achieve using tube dynamics alone. The optimal transfer obtained in the BCR4BP is compared with existing solutions to demonstrate the effectiveness of the proposed method.

The remainder of this paper is organized as follows: Section 2 describes the dynamical model of a spacecraft and related fundamental concepts. Section 3 explains lobe dynamics in detail, focusing on its application to the planar CR3BP. Section 4 presents a new method leveraging lobe dynamics for transfer trajectory design, based on Ref. [30]. Selected lobes are connected with appropriate impulsive inputs, and the overall transfer structure is summarized as a graph representing possible transfer paths. This graph enables identification of the optimal transfer connecting the start and goal orbits. Section 5 applies the proposed method to construct fuel-optimal Earth–Moon transfers. Finally, Section 6 discusses the role of lobe dynamics and the extension of the proposed method to the BCR4BP.

2. Preliminaries

This section introduces fundamental knowledge related to this study. The Earth–Moon CR3BP is mainly employed in this paper, while the Sun–Earth–Moon BCR4BP is used in Section 6 to compare the obtained results with

those in literature. Note that lobe dynamics is described separately in the next section.

2.1. Circular restricted three-body problem (CR3BP)

This subsection describes key features of the CR3BP, whose coordinate system is shown in Fig. 1. This problem considers two celestial bodies, P_1 and P_2 , and a spacecraft P_3 , all treated as point masses. Let m_1 , m_2 and m_3 denote the masses of P_1 , P_2 and P_3 , respectively, with the assumption that $m_1 > m_2 \gg m_3$. This condition means P_3 has no effect on the motion of P_1 and P_2 . Another assumption in the CR3BP is that P_1 and P_2 move in a circular orbit around their barycenter. Under these assumptions, the equations of motion of P_3 are expressed in a non-dimensional form with a pseudo-potential function U as follows:

$$\begin{cases} \ddot{x} - 2\dot{y} = \frac{\partial U}{\partial x} \\ \ddot{y} + 2\dot{x} = \frac{\partial U}{\partial y} \\ \ddot{z} = \frac{\partial U}{\partial z} \end{cases}, \quad (1)$$

$$U = \frac{1}{2} (x^2 + y^2) + \frac{1 - \mu}{r_1} + \frac{\mu}{r_2} + \frac{1}{2}\mu(1 - \mu), \quad (2)$$

$$r_1 = \sqrt{(x + \mu)^2 + y^2 + z^2}, \quad (3)$$

$$r_2 = \sqrt{\{x - (1 - \mu)\}^2 + y^2 + z^2}, \quad (4)$$

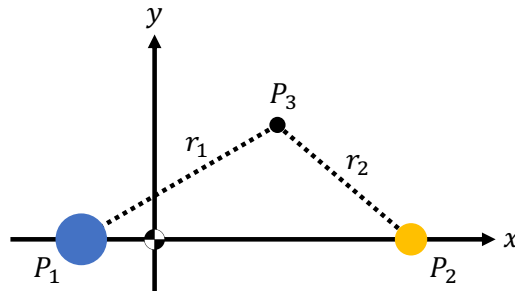


Figure 1: Coordinate system in CR3BP (Rotating frame).

where $\mu = m_2/(m_1 + m_2)$ is the non-dimensional mass ratio of the primaries, and $\mu = 1.21509 \times 10^{-2}$ in the Earth–Moon system. Note that the relatively large μ value in the Earth–Moon system leads to highly chaotic dynamics, posing challenges in trajectory design.

The CR3BP has several characteristics useful for trajectory design. First, the CR3BP has five libration points satisfying $\nabla U = \mathbf{0}$, denoted as L_i ($i = 1, 2, \dots, 5$). The dynamics around these points has been well investigated in literature (e.g., Refs. [66–68]) because each libration point L_i has families of periodic orbits. These periodic orbits and their stable and unstable manifolds are useful for analyzing the dynamics and designing trajectories. In addition, this model possesses one integral of motion, called the Jacobi constant C_J , which is defined as

$$C_J = 2U - (\dot{x}^2 + \dot{y}^2 + \dot{z}^2). \quad (5)$$

Equation (5) can be rewritten as

$$2U - C_J = \dot{x}^2 + \dot{y}^2 + \dot{z}^2 \geq 0. \quad (6)$$

This relationship shows that the condition $2U - C_J = 0$ defines the boundary of possible motion, known as the zero-velocity surface. In the planar problem, the zero-velocity surface becomes a closed curve called the zero-velocity curve. The zero-velocity curve with a given Jacobi constant divides position space into realms of possible motion [35]. The realm around the primary is referred to as the *interior realm*, and the realm around the secondary is called the *moon realm*. The realm outside both of the primaries is called the *exterior realm*. These realms can be connected through the necks around L_1 and L_2 .

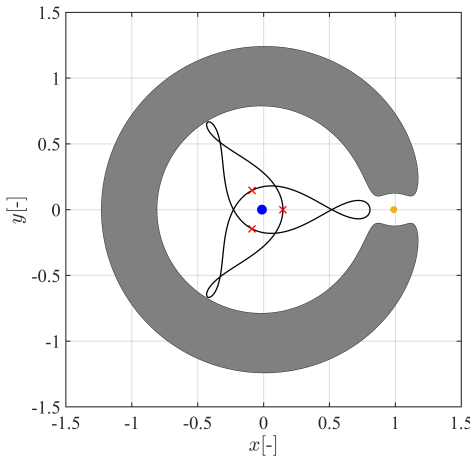
2.2. Resonant orbit

Mean-motion resonances or orbital resonances play an essential role in describing the dynamics of small bodies or spacecraft [69, 70]. In the Earth–Moon CR3BP, a $p : q$ resonant orbit ($p, q \in \mathbb{N}$) about the Earth in resonance with the Moon is defined as an orbit whose period in the inertial frame, T_3^I , is related to the sidereal period of the Moon, T_2 , as $pT_3^I \simeq qT_2$. In other words, the resonance ratio $p : q$ indicates that a spacecraft rotates around the Earth p times in approximately the same time required for the Moon to complete q revolutions [71]. If $p > q$, resonant orbits have a period less than that of the Moon and are called interior resonant orbits; if $p < q$, they are called exterior resonant orbits [72]. Since $T_3^I = 2\pi a^{3/2}/\sqrt{1-\mu}$ and $T_2 = 2\pi$

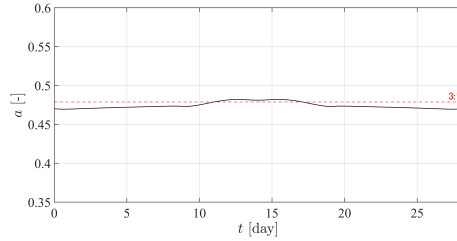
in non-dimensional units, the semi-major axis a of the resonance orbit is expressed as

$$a \simeq \left(\frac{q}{p} \right)^{2/3} (1 - \mu)^{1/3}. \quad (7)$$

Figure 2 illustrates a 3:1 unstable resonant orbit and the time history of its semi-major axis. The red crosses indicate periapses of this resonant orbit, and the blue and yellow dots represent the Earth and Moon, respectively. The gray region is the forbidden realm where $2U - C_J < 0$. As shown in Fig. 2(b), the semi-major axis roughly satisfies Eq. (7), as represented by the red dashed line. The perturbation of the semi-major axis comes from the gravitational influence of the Moon. Resonant orbits have planar [73] and spatial [71]



(a) In the x - y plane.



(b) Time history of the semi-major axis along the orbit.

Figure 2: Example of a resonant orbit (the 3:1 unstable resonant orbit when $C_J = 3.16$) and its semi-major axis.

families, and quasi-periodic tori may exist around these orbits [74]. These orbits are useful in trajectory design [75, 76], as has been demonstrated by the extended mission of IBEX [77] and the TESS mission [78].

Interesting transitions between orbits with different resonance ratios, called resonance transitions [25, 39, 79], have been observed for short-period comets such as Oterma. Resonance transitions, also referred to as resonant hopping [80, 81] or resonant gravity assists [82, 83], are useful in trajectory design, especially for a tour design in multi-moon systems [84, 85]. In this phenomenon, weak capture at the Moon plays a significant role [79], where the Kepler energy around the Moon is non-positive in multi-body dynamics. Figure 3 illustrates the resonance transition from 2:1 to 1:3 in the rotating frame and in the Earth-centered inertial frame. The region where weak capture occurs is defined as the weak stability boundary (WSB), which was first introduced by Belbruno [86] and has been extended in Ref. [79]. The WSB can be regarded as a more general and precise estimation of the sphere of influence in multi-body dynamics [87].

2.3. Periapsis Poincaré map

This study focuses on lobes divided by the stable and unstable manifolds of resonant orbits. The geometry of these manifolds is complex in the position space, and therefore periapsis Poincaré maps are utilized to understand

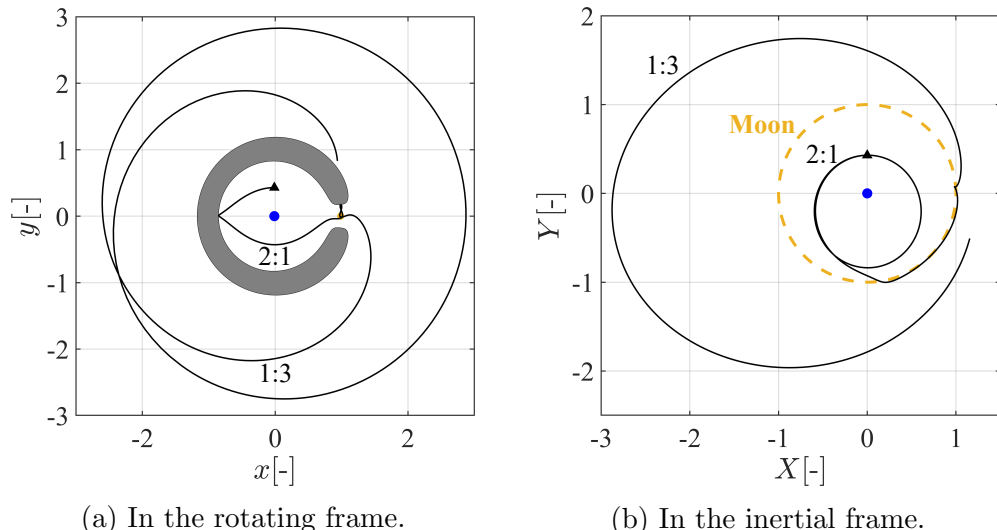


Figure 3: Example of resonance transition in the Earth-Moon CR3BP [79].

the dynamics. The periapsis Poincaré map is a Poincaré map whose surface of section lies in periapsis passage. This idea was first introduced for astrodynamics in Ref. [88]. One of its advantages is enabling the projection of dynamical structures onto position space, which is applied to design transfer trajectories [31, 89]. This study extracts dynamical structures related to resonances by numerically constructing a periapsis Poincaré map in the Delaunay elements [90]. These elements are canonical and suitable for analyzing lobe dynamics.

Periapses are calculated with respect to the Earth (i.e., $\dot{r}_1 = 0$ and $\ddot{r}_1 > 0$) throughout this paper. The following coordinate transformation is necessary to obtain periapsis Poincaré maps in the Delaunay elements. First, the temporary inertial frame, the X - Y frame, is defined so that its axes coincide with those of the rotating x - y frame, and its origin is located at the Earth. Specifically, the relationship between the X - Y frame and the x - y plane is expressed as

$$\begin{bmatrix} X \\ Y \\ \dot{X} \\ \dot{Y} \end{bmatrix} = \begin{bmatrix} 1 & 0 & 0 & 0 \\ 0 & 1 & 0 & 0 \\ 0 & -1 & 1 & 0 \\ 1 & 0 & 0 & 1 \end{bmatrix} \begin{bmatrix} x + \mu \\ y \\ \dot{x} \\ \dot{y} \end{bmatrix}. \quad (8)$$

On this inertial frame, classical orbital elements for the planar problem (the semi-major axis a , eccentricity e , argument of periapsis ω , and true anomaly f) are defined such that

$$a = \frac{(1 - \mu) r_1}{2(1 - \mu) - r_1 V^2}, \quad (9)$$

$$\mathbf{e} = -\frac{(\mathbf{r}_1 \times \mathbf{V}) \times \mathbf{V}}{1 - \mu} - \frac{\mathbf{r}_1}{r_1}, \quad e = \|\mathbf{e}\|, \quad (10)$$

ω is the angle from the X axis to the \mathbf{e} vector, and f is the angle from the \mathbf{e} vector to the \mathbf{r}_1 vector, where

$$\mathbf{r}_1 = \begin{bmatrix} X \\ Y \\ 0 \end{bmatrix}, \quad r_1 = \|\mathbf{r}_1\|, \quad \mathbf{V} = \begin{bmatrix} \dot{X} \\ \dot{Y} \\ 0 \end{bmatrix}, \quad V = \|\mathbf{V}\|. \quad (11)$$

Figure 4 illustrates these orbital elements on the X - Y frame. Note that this transformation assumes that the inclination of the elliptic orbit is zero and the angular momentum is positive, i.e., $X\dot{Y} - Y\dot{X} > 0$.

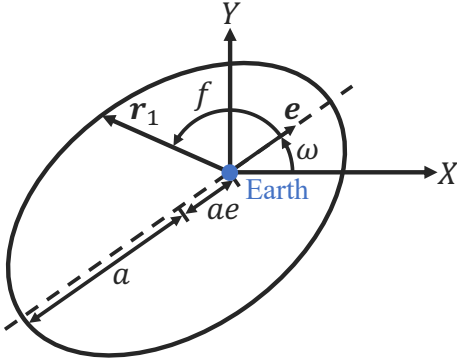


Figure 4: Classical orbital elements for an elliptic orbit in the temporary inertial frame (when $X\dot{Y} - Y\dot{X} > 0$).

The orbital elements (a, e, ω, f) are converted to the Delaunay elements (l_d, g_d, L_d, G_d) as follows:

$$l_d = M = E - e \sin E, \quad (12)$$

$$g_d = \omega, \quad (13)$$

$$L_d = \sqrt{(1 - \mu) a}, \quad (14)$$

$$G_d = \sqrt{(1 - \mu) a (1 - e^2)}, \quad (15)$$

where G_d is identical to the magnitude of the angular momentum $h = |X\dot{Y} - Y\dot{X}|$, M is the mean anomaly, and E is the eccentric anomaly satisfying

$$E = 2 \tan^{-1} \left(\sqrt{\frac{1 - e}{1 + e}} \tan \frac{f}{2} \right). \quad (16)$$

Periapsis passage corresponds to $f = 0$, which is equal to $l_d = 0$ from Eqs. (12) and (16) when $0 < e < 1$.

In this paper, the periapsis Poincaré map is defined as $l_d = 0$ ($X\dot{Y} - Y\dot{X} > 0$) in the canonical g_d - G_d plane and illustrated in Fig. 5. The four-dimensional phase space in the planar CR3BP is reduced to two-dimensional Poincaré maps by taking a surface of section (periapsis passage for Fig. 5) and fixing the Jacobi constant ($C_J = 3.16$ for this case). On this map, the phase space can be divided into *resonance regions* [35, 91] and *chaotic zones*. The former includes quasi-periodic and periodic orbits, while the latter consists of chaotic orbits.

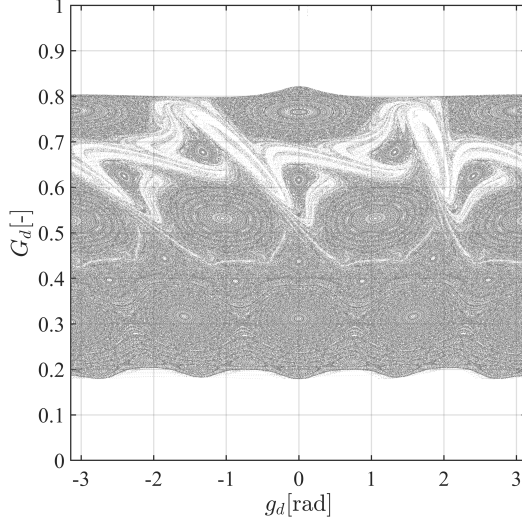


Figure 5: Periapsis passage points on the Poincaré section for the Earth–Moon system ($l_d = 0$, $X\dot{Y} - Y\dot{X} > 0$, and $C_J = 3.16$).

2.4. Bicircular restricted four-body problem (BCR4BP)

This subsection briefly introduces the BCR4BP, one of the models for the Sun–Earth–Moon system. The BCR4BP is the simplest model for this four-body system, assuming that the Sun S moves around the barycenter of the Earth–Moon rotating frame in a circular orbit. Its coordinate system is shown in Fig. 6. The Sun is often assumed to be on the Earth–Moon orbital plane. The position of the Sun is then written as

$$x_s = a_s \cos \theta_s, \quad y_s = a_s \sin \theta_s, \quad z_s = 0, \quad (17)$$

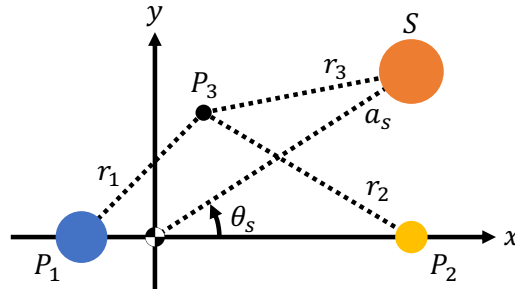


Figure 6: Coordinate system in BCR4BP (Earth–Moon rotating frame).

where a_s is the non-dimensional distance between the Sun and the barycenter of the Earth–Moon system (3.89173×10^2 [-]), and θ_s is the phase angle of the Sun, given by

$$\theta_s = \theta_s^* + \omega_s t. \quad (18)$$

Note that θ_s^* is the initial value of θ_s , ω_s is the non-dimensional angular velocity of the Sun, defined as $\omega_s = \sqrt{(1 + m_s)/a_s^3} - 1$, and m_s is the non-dimensional mass of the Sun (3.28914×10^5 [-]). Thus, the BCR4BP is time-dependent, and the Earth–Moon system is periodically perturbed by the Sun.

Under these assumptions, the non-dimensional equations of motion of P_3 are expressed with a pseudo-potential function Υ based on Eq. (1) as follows:

$$\begin{cases} \ddot{x} - 2\dot{y} = \frac{\partial \Upsilon}{\partial x} \\ \ddot{y} + 2\dot{x} = \frac{\partial \Upsilon}{\partial y} \\ \ddot{z} = \frac{\partial \Upsilon}{\partial z} \end{cases}, \quad (19)$$

$$\Upsilon = \frac{1}{2} (x^2 + y^2) + \frac{1 - \mu}{r_1} + \frac{\mu}{r_2} + \frac{m_s}{r_s} - \frac{m_s}{a_s^3} (x_s x + y_s y + z_s z), \quad (20)$$

$$r_s = \sqrt{(x - x_s)^2 + (y - y_s)^2 + (z - z_s)^2}. \quad (21)$$

When $m_s \rightarrow 0$, Eq. (1) of the CR3BP is recovered from Eq. (19) of the BCR4BP.

3. Lobe dynamics

This section introduces the idea of extracting lobes suitable for guiding a spacecraft in chaotic zones [30]. In the planar CR3BP, the stable and unstable manifolds of a resonant orbit may form regions called lobes. Lobe dynamics describes the chaotic transport of phase space volume between lobes within a single realm. A detailed explanation of lobe dynamics for trajectory design is given below.

3.1. Description of lobe dynamics for trajectory design

Consider hyperbolic fixed points (p_1 and p_2) on a two-dimensional, area- and orientation-preserving map F (see Fig. 7). Examples of F include the standard map and a Poincaré map in the planar CR3BP. On the map F , it is assumed that an unstable manifold of p_1 , $W_{p_1}^u$, and a stable manifold of p_2 , $W_{p_2}^s$, form a heteroclinic tangle (or a homoclinic tangle when $p_1 = p_2$). Heteroclinic and homoclinic points are defined as follows:

Definition 1 (Heteroclinic/homoclinic point). A point q_i on the map F is called a *heteroclinic point* if $q_i \in W_{p_1}^u \cap W_{p_2}^s$. If $p_1 = p_2$, then q_i is called a *homoclinic point*.

To describe lobes and lobe dynamics, primary intersection points are defined as follows:

Definition 2 (Primary intersection point, pip [43]). Consider a heteroclinic/homoclinic point $q_i \in W_{p_1}^u \cap W_{p_2}^s$. The segment of $W_{p_1}^u$ from X to Y and the segment of $W_{p_2}^s$ from X to Y are denoted as $U[X, Y]$ and $S[X, Y]$, respectively. Then, q_i is called a *primary intersection point* if $U[p_1, q_i]$ and $S[p_2, q_i]$ intersect only in q_i (and possibly in p_1 when q_i is a homoclinic point). In Fig. 7, all the black dots represent pips.

Lobes are then defined as follows:

Definition 3 (Lobe [43]). Let q_0 and q_1 be adjacent pips, i.e., no other pips exist on $U[q_0, q_1]$ and $S[q_0, q_1]$. A *lobe* is defined as a region bounded by $U[q_0, q_1]$ and $S[q_0, q_1]$.

The transport structure of lobes, called *lobe dynamics*, is governed by the map F . For example, the lobe bounded by $U[q_0, q_1]$ and $S[q_0, q_1]$ is mapped

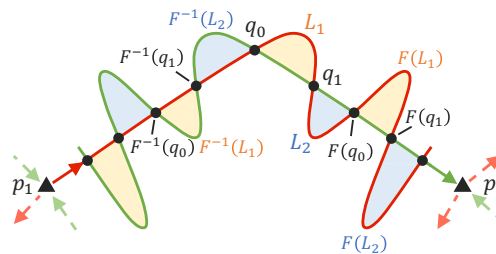


Figure 7: General description of lobes.

to the lobe bounded by $U[F(q_0), F(q_1)]$ and $S[F(q_0), F(q_1)]$. Specific lobes moving into/out of resonance regions under one mapping of F (e.g., $F^{-1}(L_2)$ and $F^{-1}(L_1)$ in Fig. 7) are called *turnstiles* [44, 45, 92], which govern the transport between resonance regions and chaotic zones.

A series of lobes mapped by F is called a *lobe sequence*, which is introduced in Ref. [30] and defined as follows:

Definition 4 (Lobe sequence [30]). Assume that a lobe L exists on the map F . A sequence

$$\{\cdots, F^{-n}(L), \cdots, F^{-1}(L), L, F(L), \cdots, F^n(L), \cdots\},$$

for $\forall n$ is called a lobe sequence $\Lambda(F, L)$.

In Fig. 7, the stable and unstable manifolds form two lobe sequences

$$\{\cdots, F^{-1}(L_1), L_1, F(L_1), \cdots\} \text{ (a sequence of the yellow lobes),}$$

and

$$\{\cdots, F^{-1}(L_2), L_2, F(L_2), \cdots\} \text{ (a sequence of the blue lobes).}$$

The number of lobe sequences depends on pairs of manifolds dividing the phase space into lobes.

It is difficult to visualize the entire picture of a lobe sequence because the accurate and extended propagation of the stable and unstable manifolds is necessary to detect finer lobes in the sequence. In this study, this numerical difficulty is avoided by leveraging *effective lobes* [30]. First, the *radius of a lobe* is defined as follows:

Definition 5 (Radius of a lobe [30]). The ε -ball is an open ball whose radius is $\varepsilon \in \mathbb{R}$ ($\varepsilon > 0$), defined as:

$$B_\varepsilon(\mathbf{c}) := \{\boldsymbol{\xi} \in \mathbb{R}^2 : \|\boldsymbol{\xi} - \mathbf{c}\| < \varepsilon\},$$

where $\boldsymbol{\xi}$ is the state on the map F , and $\mathbf{c} \in \mathbb{R}^2$ is the center of this ball. The radius of a lobe is the maximum radius of ε -ball contained within a lobe region L_i , defined as:

$$r_{L,i} := \max_{\mathbf{c} \in L_i, B_\varepsilon(\mathbf{c}) \subset L_i} \varepsilon.$$

For simplicity, the radius of a lobe $r_{L,i}$ is calculated as the minimum distance between the centroid of a lobe and its boundary (see Fig. 8). Now, the *effective lobes* and *effective lobe sequences* are defined using a threshold radius r_L^* for robust transfer design.

Definition 6 (Effective lobe [30]). An effective lobe is defined as a lobe whose radius satisfies the condition

$$r_{L,i} > r_L^*,$$

where r_L^* is the threshold value for the radius of lobes.

Definition 7 (Effective lobe sequence [30]). A finite lobe sequence $\Lambda(F, L, r_L^*) \subset \Lambda(F, L)$ in which all lobes are effective lobes satisfying $r_{L,i} > r_L^*$ and are selected in order from the sequence $\Lambda(F, L)$ is called an *effective lobe sequence* with respect to r_L^* .

To investigate the transport structure between lobe sequences, this study assumes that the transfers between lobes (region-to-region transfer) are represented by transfers between the centroids of the lobes (point-to-point transfer). Under this assumption, effective lobes allow errors whose size is less than r_L^* (e.g., control errors and/or orbit determination errors). Despite such errors, spacecraft will remain within effective lobes, and the transfer between effective lobes becomes robust.

3.2. Lobe sequences in the CR3BP

This subsection describes effective lobe sequences in the planar Earth–Moon CR3BP. The 7:2 and 3:1 unstable resonant orbits are selected for trajectory design because the corresponding resonance regions are relatively large in Fig. 5 and their lobe dynamics is considered to enhance phase space

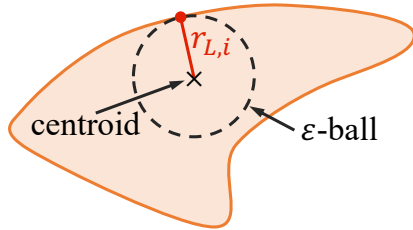


Figure 8: Illustration of the radius of a lobe for computation.

transport. The initial guesses for these resonant orbits can be obtained by a grid search on the Poincaré map, and the exact initial conditions are acquired through the differential correction method [93]. By propagating the stable and unstable manifolds of the obtained resonant orbits, heteroclinic tangles on the Poincaré map are revealed. Based on the heteroclinic tangles, one can find the initial guesses for pips. Pips are precisely identified by parameterizing the manifolds and calculating their crossing points. The lobes are determined by the adjacent pips and the manifolds connecting them. Thus, parameterizing the manifolds makes it easier to detect lobe boundaries. Once a lobe in a certain lobe sequence is found, the whole lobe sequence can be revealed by propagating the boundary of the lobe forward and backward in time.

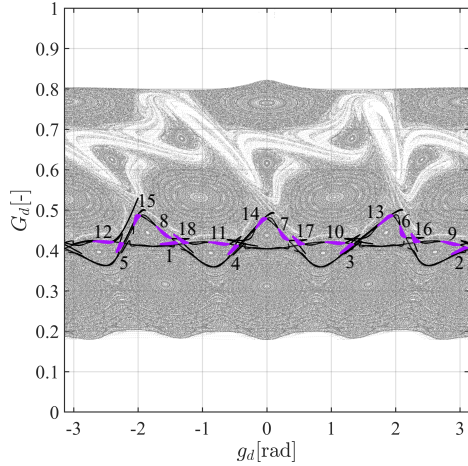
Figure 9 demonstrates effective lobes when $r_L^* = 0.002$ in the selected lobe sequences. In Fig. 9, the name of a lobe sequence, $LX.Y$, indicates the Y -th lobe sequence of the X -th periodic orbit. Here, the first orbit is the 7:2 unstable resonant orbit, and the second orbit is the 3:1 unstable resonant orbit. The number in Fig. 9 shows the order of transfers in the lobe sequence.

4. Trajectory design based on lobe dynamics

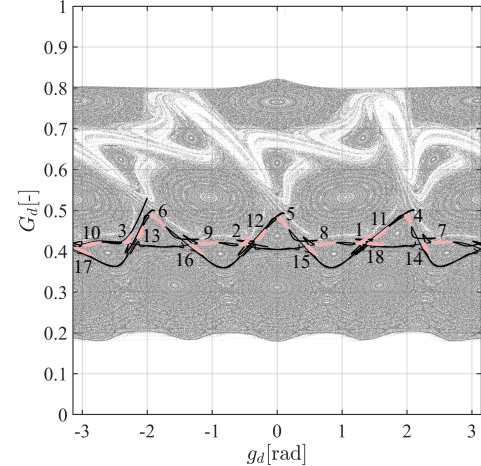
This section describes the proposed method for designing low-energy chaotic transfers based on lobe dynamics. Effective lobe sequences are utilized to predict the motion of chaotic orbits within lobes. The selected chaotic orbits are connected by impulsive maneuvers to construct a low-energy transfer. These maneuvers help to overcome the partial barriers [45] formed by cantori [92] or the boundaries of resonance regions in the periapsis Poincaré map of the planar CR3BP. In the following sections, the threshold radius for effective lobes is fixed at $r_L^* = 0.002$ as a representative example.

Indeed, natural trajectories passing through different lobe sequences exist due to the chaotic dynamics, as demonstrated by Odashima *et al.* [61] using a gridded search within a lobe associated with the 3:1 resonant orbit. The proposed method, however, connects different lobe sequences with small maneuvers in order to simplify the low-energy transfer design process. This simplification enables choosing more resonant orbits for incorporating lobe sequences.

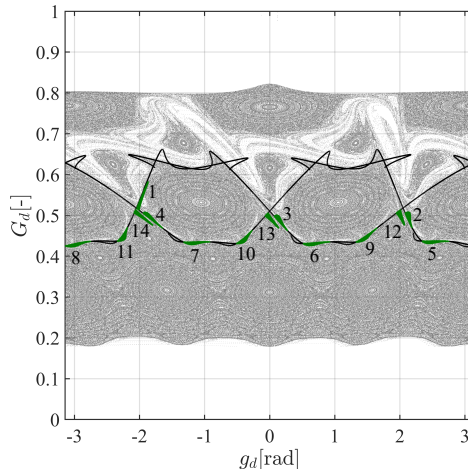
The main idea of the proposed method is to utilize a weighted, directed graph to search for the fuel-optimal transfer path. After discretizing the



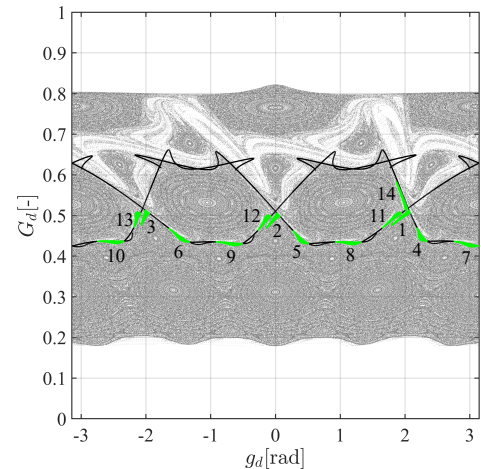
(a) L1.1



(b) L1.2

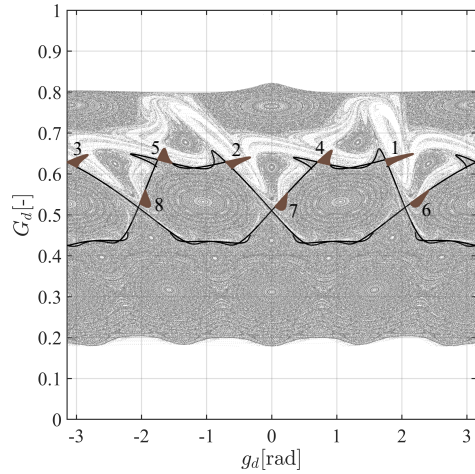


(c) L2.1

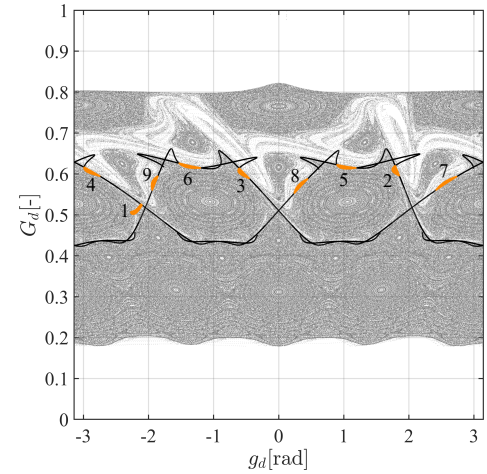


(d) L2.2

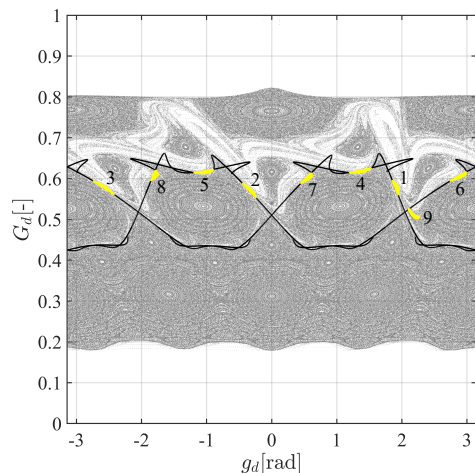
Figure 9: Effective lobe sequences in the planar Earth–Moon CR3BP.



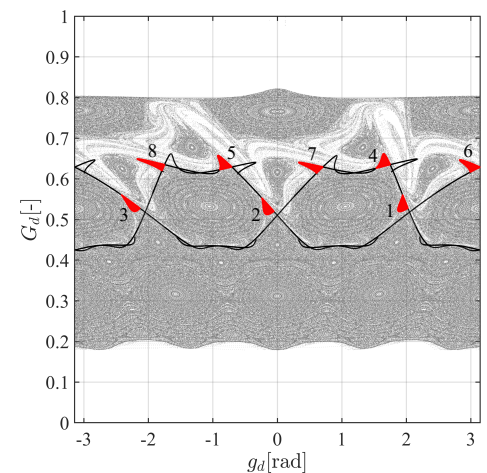
(e) L2.3



(f) L2.4



(g) L2.5



(h) L2.6

Figure 9: Effective lobe sequences in the planar Earth–Moon CR3BP. (Continued)

solution space, such a graph-based framework is suitable for representing potential impulsive transfer paths. The graph structure aids in solving combinatorial optimization over a set of natural arcs, such as periodic orbits and their manifolds [94, 95], or a set of motion primitives [96]. Similarly, Oshima [97] represents the solution space using a set of periapsis-to-periapsis arcs for low-energy transfers. This study constructs periapsis-to-periapsis arcs in a simpler manner and focuses on the optimal combination of effective lobe sequences.

4.1. Overview of the design method

Transfer design with effective lobe sequences requires determining the combination of the lobe sequences and the timing for a spacecraft to enter and leave them to minimize the transfer cost. To this end, the proposed method leverages a weighted, directed graph with three components: nodes (discrete state points), directed edges (transfer paths), and weights (transfer costs). In the graph, nodes stand for potential start and goal points as well as for the centroids of the effective lobes in Fig. 9. The edges connecting these nodes indicate allowable transfer paths, which are predesigned based on their dynamical geometry. The weight of each edge is assigned as the corresponding transfer cost, such as ΔV or the transfer time. Figure 10 illustrates a schematic diagram of the graph for the proposed method. The triangle, dots, and star indicate the start node, the nodes corresponding to effective lobes, and the goal node, respectively. The directed arrows show

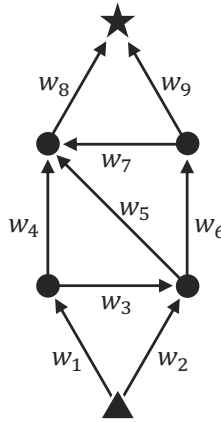


Figure 10: A schematic diagram of the weighted, directed graph for impulsive transfer design.

predesigned edges, and the edge weights are denoted by w_k ($k = 1, 2, \dots, 9$). The detailed procedure for designing transfer trajectories corresponding to the edges is examined using a test problem in the following subsections.

The optimal transfer is determined by exhaustive search, which computes the total weight for all possible transfers from the start nodes to the goal nodes. The combinatorial optimization problem can be formulated as follows:

$$\text{minimize} \quad J = \sum_k w_k \quad (22)$$

$$\text{subject to} \quad w_k < w^*, \quad (23)$$

$$\text{“Use lobe sequences properly,”} \quad (24)$$

where J is the sum of w_k along a transfer path from one of the start nodes to one of the goal nodes, and w^* is a weight threshold. The number of the combinations is reduced by only considering edges whose weight satisfies Eq. (23). The second constraint of Eq. (24) implies that if a spacecraft goes through one of the lobe sequences, at least two adjacent lobes in the lobe sequence must be included in the transfer path (see Fig. 11). This constraint requires the full exploitation of lobe dynamics during transfers, which demonstrates the effectiveness of the approach. Note that this condition can be neglected for mission design.

4.2. Test problem settings

A test problem for the fuel-optimal transfer is considered to investigate the design of each transfer arc and its corresponding weight. In this problem, the departure orbit and destination are defined within the periapsis Poincaré map, as summarized in Fig. 12. The departure orbit is the 7:2 stable resonant orbit in Fig. 13, and the triangles in Figs. 12 and 13 indicate its periapses.

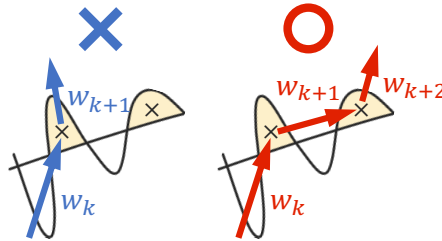


Figure 11: Illustration of the constraint Eq. (24).

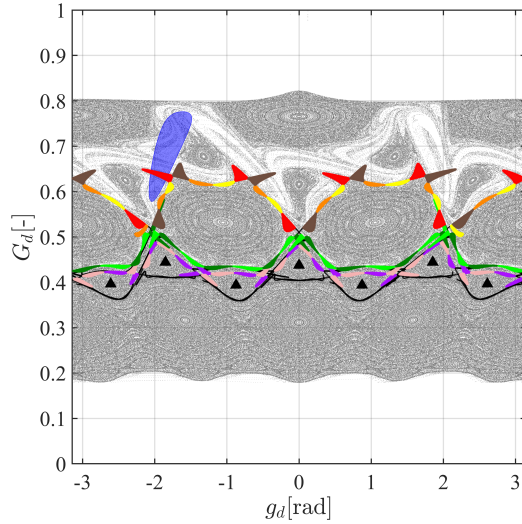


Figure 12: Problem settings for the test problem.

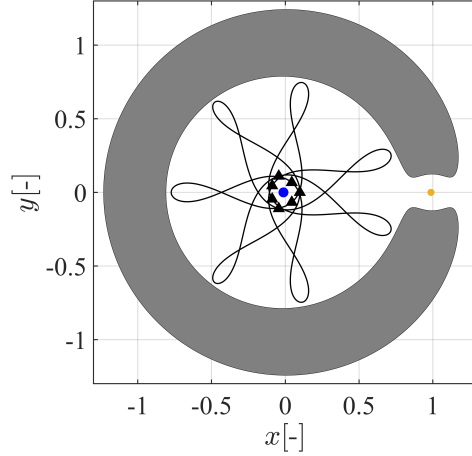


Figure 13: The 7:2 stable resonant orbit when $C_J = 3.16$.

It is noteworthy that the altitudes of these periapses to the Earth are from 27,279 km to 37,746 km, implying that the starting points exist roughly around the geosynchronous Earth orbit (GEO) [90] since the altitude of the GEO is about 35,780 km. The destination is defined as the left half of the stable manifold of the L_1 Lyapunov orbit, as shown in Fig. 14. The black line is the L_1 Lyapunov orbit, and the green lines represent its stable manifold. The blue regions in Figs. 12 and 14 illustrate the first intersection

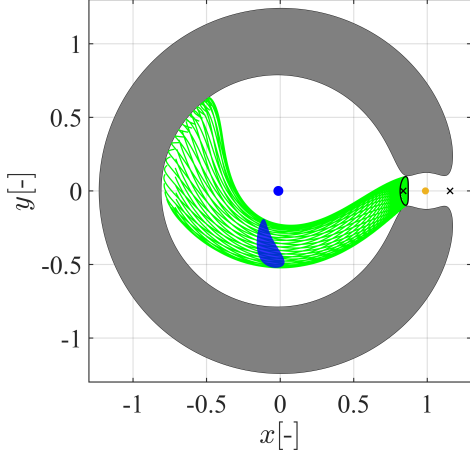


Figure 14: The left half of the stable manifold of the L_1 Lyapunov orbit when $C_J = 3.16$.

to the periapsis Poincaré map. These blue regions can be regarded as the exit to the moon realm, as a spacecraft within them is delivered to the Moon or possibly to deep space via tube dynamics. The other colored regions in Fig. 12 represent the selected effective lobe sequences corresponding to those in Fig. 9. Thus, this test problem aims to design a low-energy, fuel-optimal transfer for escaping from the Earth.

In a graph for this test problem, nodes stand for the periapses of the departure orbit and the centroids of the selected effective lobes. The goal node is defined as the centroid of the eighth effective lobe in L2.6 in Fig. 9(h) because this lobe overlaps the blue region of the destination in Fig. 12. Edges connecting these nodes are constructed as shown in Fig. 15. These edges are designed so that a spacecraft can monotonically increase G_d . The name and

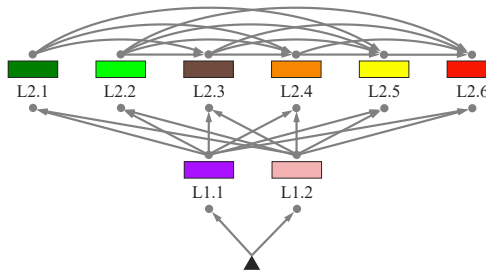


Figure 15: Design of transfer paths for the test problem.

color in Fig. 15 correspond to those of the lobe sequences in Fig. 9, and the triangle shows the start nodes. The arrows indicate possible transfer paths. For example, the arrow from L1.1 to L2.2 means that the graph includes transfer paths from each effective lobe in L1.1 to each effective lobe in L2.2.

In the proposed method, it is essential to define the way of designing transfer arcs corresponding to the edges and evaluating their weights. For the edges from the start nodes to the lobes or from one lobe sequence to another, i.e., the edges for controlled transfers, transfer arcs are simply designed by so-called targeting [98], as shown in Fig. 16. When making a transfer from \mathbf{x}_1 to \mathbf{x}_2 , for example, a crossing point in the position space is detected by propagating \mathbf{x}_1 forward over time interval $[0, 2\pi]$ and \mathbf{x}_2 backward over time interval $[0, -2\pi]$. An impulsive $\Delta\mathbf{V}$ is applied at this crossing point to adjust the direction of the velocity and keep the Jacobi constant. The weight for this transfer arc is defined as the magnitude of this $\Delta\mathbf{V}$. For the edges between lobes in the same lobe sequence, i.e., the edges for transfers based on natural dynamics, two cases are considered in this test problem:

- *Case 1: Without targeting.* Transfer arcs are determined by propagating the initial point \mathbf{x}_1 until it reaches the lobe containing \mathbf{x}_2 . The corresponding weight is zero, but the value of \mathbf{x}_2 is updated to the actual final point after the propagation.
- *Case 2: With targeting.* Transfer arcs and their weights are determined by the targeting method shown in Fig. 16. The weights are generally small because the transfer arcs are based on lobe dynamics.

In all the cases, the value of w^* is set as 100 m/s so that solutions containing infeasible paths are ignored during the optimization.

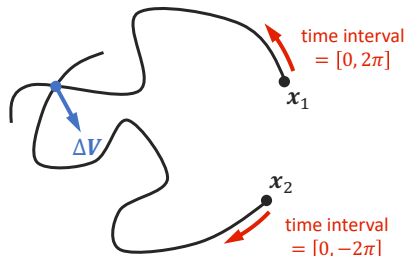


Figure 16: Illustration of the way of building an impulsive transfer arc.

4.3. Test results

Test results for all paths in both cases are summarized in Table 1 and Fig. 17. The effect of the constraint of Eq. (24) is also examined. The label “Estimated” indicates that the total costs are estimated by assuming that the edge weights for transfers based on lobe dynamics are precisely zero. The label “Without targeting” denotes that the total costs are determined by the graph in Case 1. The last label “With targeting” represents that the total costs are calculated from the graph in Case 2. Table 1 indicates the number of transfers found by the three approaches. In Case 1 (without targeting), some transfer paths do not yield the corresponding transfer trajectories because controlled transfer arcs fail to be reconstructed as a result of the propagation. In contrast, in Case 2 (with targeting), all transfer paths generate transfer trajectories due to the targeting strategy. The constraint of Eq. (24) reduces the number of transfers found, regardless of the difference between the approaches. Next, Fig. 17 shows swarm charts of the total transfer costs determined by the three approaches. A swarm chart displays each data point individually, clearly illustrating the distribution of discrete data. Figures 17(c) and 17(d) highlight low-cost transfers in Figs. 17(a) and 17(b), respectively. Figure 17 illustrates that transfer costs in Case 1 (without targeting) are significantly different from the estimated values. In Case 2 (with targeting), transfer costs have a distribution similar to the estimated values. Thus, the targeting strategy is practical for realizing transfer trajectories from the graph structure in the proposed method. The comparison between Fig. 17(a) and Fig. 17(b), and between Fig. 17(c) and Fig. 17(d) reveals that the number of transfers found is reduced by the constraint of Eq. (24), but their distribution does not change significantly.

For both Cases 1 and 2, the optimal transfer paths are shown in Fig. 18. The black triangle and dots represent the start point and the centroids of the selected lobes, respectively. The numbers indicate the order of transfer. Figure 19 depicts the corresponding optimal transfer trajectories. The black lines show the segments of the departure orbit, blue arrows indicate $\Delta\mathbf{V}$ vectors, and the other colored lines represent natural trajectories within effective lobes (their color corresponds to that of the lobe sequences in Fig. 9). The size of the blue arrows is adjusted within the same figure and cannot be compared to that in a different figure. In Case 1, the estimated total cost is small, but the total cost of the realized trajectory becomes larger in Fig. 19(a) due to propagation errors. These propagation errors are caused by numerical errors in determining the boundaries and centroids of lobes.

Table 1: Number of transfers found by different approaches from Fig. 15.

	Estimated	Without targeting	With targeting
Without Eq. (24)	544	528	544
With Eq. (24)	388	376	388

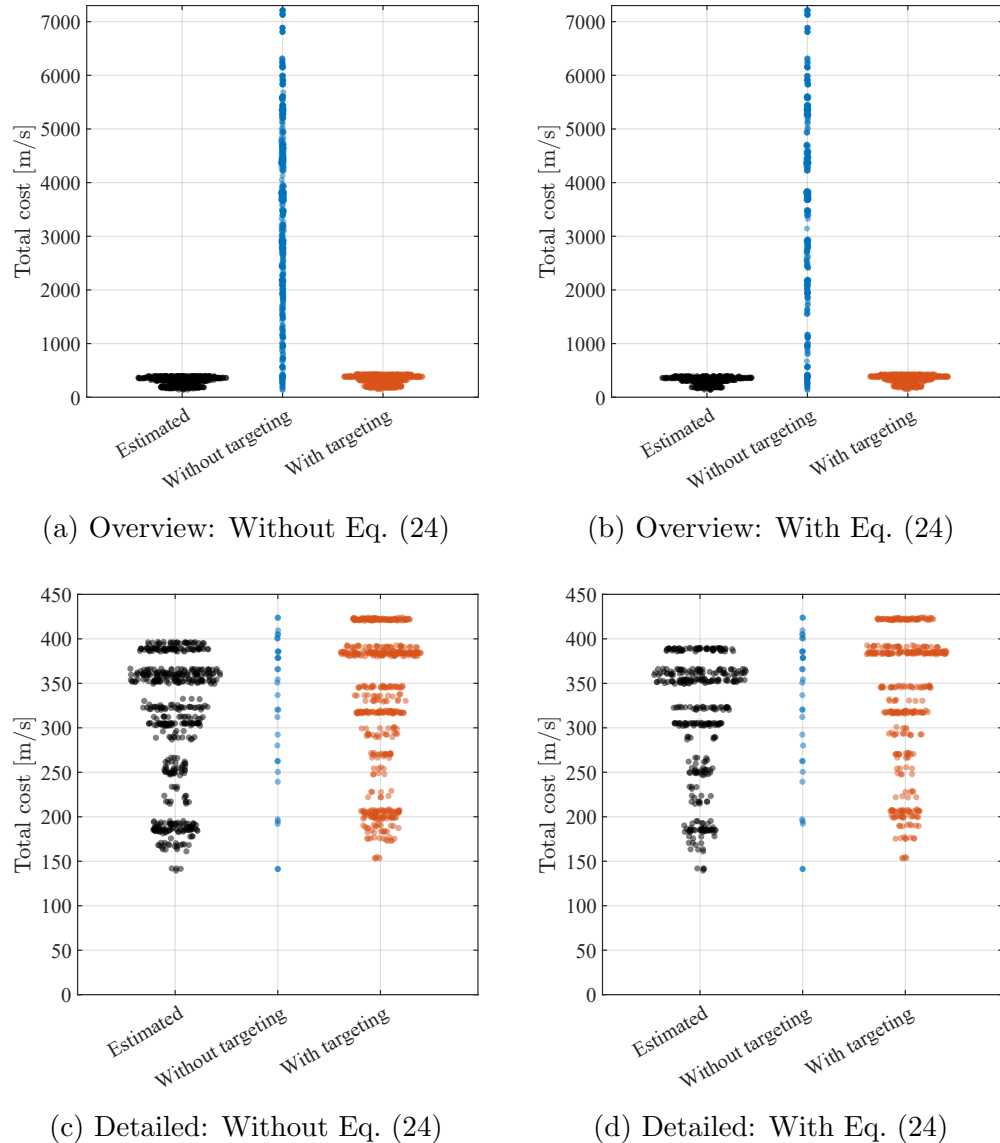
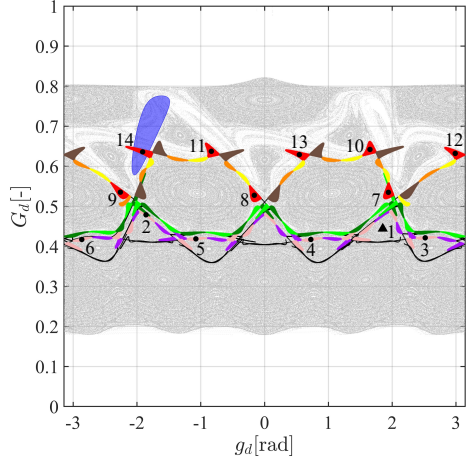
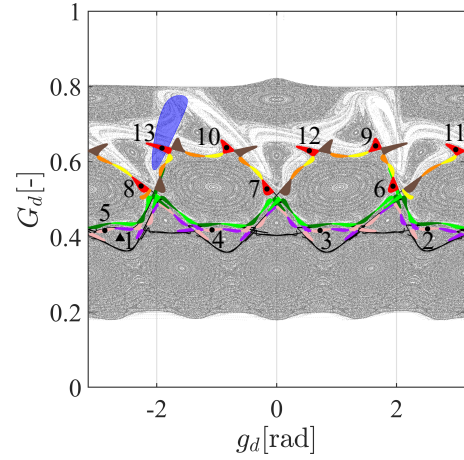


Figure 17: Swarm chart for the transfer costs of all potential paths with different approaches.

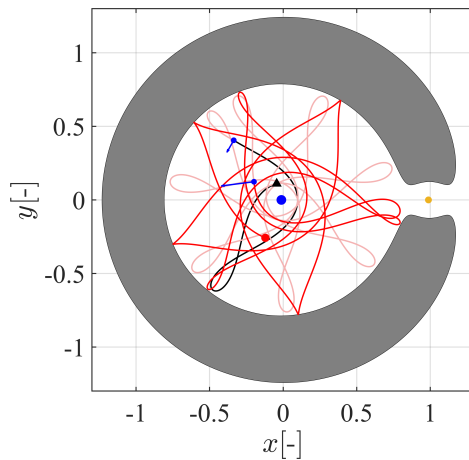


(a) Without targeting (Estimated total $\Delta V = 139.5308$ m/s)

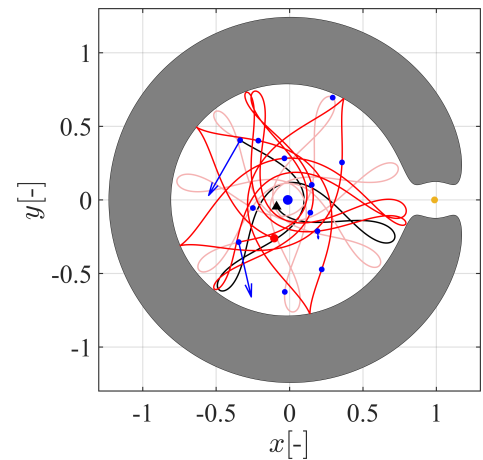


(b) With targeting (Total $\Delta V = 153.2523$ m/s)

Figure 18: Optimal transfer paths in the periapsis Poincaré map for Cases 1 and 2.



(a) Without targeting (Total $\Delta V = 250.4744$ m/s)



(b) With targeting (Total $\Delta V = 153.2523$ m/s)

Figure 19: Optimal transfer trajectories for Cases 1 and 2.

In Case 2, the propagation errors are corrected by small maneuvers with $|\Delta\mathbf{V}| < 9$ m/s, and as a result, the desired transfer trajectory is constructed with a small total cost.

In summary, the obtained results suggest that the constraint of Eq. (24) does not drastically change total transfer costs and that the approach of Case 2 is preferable for determining transfer arcs and the corresponding weights.

5. Application to Earth–Moon transfer in the CR3BP

The proposed method is applied to a more realistic mission scenario, i.e., Earth–Moon transfers in the planar CR3BP [99]. Specifically, the transfer from the low Earth orbit (LEO) to the low lunar orbit (LLO) is considered.

5.1. Earth–Moon transfer design

In this study, the LEO is defined by a circular orbit around the Earth with an altitude of 167 km, and the LLO is a circular orbit around the Moon with an altitude of 100 km. These circular orbits are discretized equally into 12 points. The angles between the x axis and each point at the LEO and LLO, denoted as θ_{LEO} and θ_{LLO} , are given by $\theta_{\text{LEO}}, \theta_{\text{LLO}} = k\pi/6$ ($k = 0, 1, \dots, 11$). As intermediate points of transfer, the centroids of the effective lobes in Fig. 9 are used, similar to the test problem in Section 4.2. The $\Delta\mathbf{V}$ s are performed to connect transfer arcs between the start points at the LEO, the effective lobes, and the goal points at the LLO. The first transfer arc includes the $\Delta\mathbf{V}$ for departure from the LEO, $\Delta\mathbf{V}_E$, which is applied tangentially to set the Jacobi constant to $C_J = 3.16$. The last transfer arc contains the $\Delta\mathbf{V}$ for insertion into the LLO, $\Delta\mathbf{V}_M$, which is applied tangentially to change C_J to the value at the goal point. In this problem, tube dynamics is not explicitly utilized, but effective lobes and the LLO are connected through tubes implicitly.

To build a graph for this problem, the nodes corresponding to the start points, centroids of the effective lobes, and goal points are connected by edges, as shown in Fig. 20. The arrows indicate possible transfer paths, and a spacecraft can move from any selected effective lobe sequence to the LLO. Transfer arcs and their weights are determined by the targeting strategy shown in Fig. 16. The $|\Delta\mathbf{V}_E|$ and $|\Delta\mathbf{V}_M|$ are added to the cost function J in Eq. (22) when the total transfer cost is evaluated. The weight threshold w^* is set to 400 m/s based on the graph structure in this case.

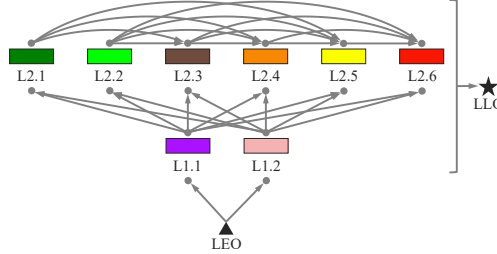


Figure 20: Design of transfer paths for the Earth–Moon transfer.

As a result, the graph for the optimization is obtained as shown in Fig. 21. The triangles and stars represent the start and goal points, respectively. The colored dots indicate the centroids of the selected effective lobes, and their color corresponds to that of the lobe sequences in Fig. 9. The gray arrows represent possible transfer paths whose weight satisfies $w < w^*$. This graph is utilized to solve the optimization problem by exhaustive search.

5.2. Obtained results in the CR3BP

The proposed method yields the optimal Earth–Moon transfer with a total ΔV of 4274.6742 m/s and transfer time of 191.8994 days, as shown in

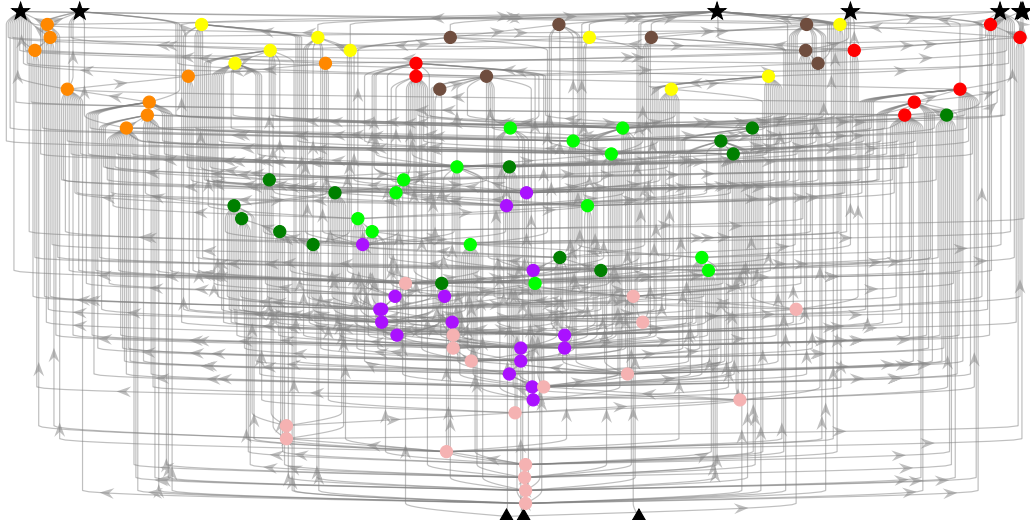


Figure 21: Graph representing possible transfer paths for the Earth–Moon transfer when $w^* = 400$ m/s.

Fig. 22. Figure 22(a), similar to Fig. 18, shows the optimal transfer path in the periapsis Poincaré map. Figure 22(b), similar to Fig. 19, illustrates the corresponding optimal transfer trajectory. The black trajectories are the transfer arcs departing from the LEO and arriving at the LLO. As a result of the optimization, the start and goal points are set as $\theta_{\text{LEO}} = \pi/3$ and $\theta_{\text{LLO}} = 5\pi/3$, respectively. The four largest ΔV s contribute to the majority of the total ΔV . Specifically, $|\Delta V_E| = 3102.2013$ m/s is applied to depart the LEO, $|\Delta V| = 398.9009$ m/s is added to move into the purple lobe sequence, $|\Delta V| = 102.6439$ m/s is added to escape from the red lobe sequence toward the LLO, and $|\Delta V_M| = 636.4582$ m/s is finally performed to arrive at the LLO. The other small ΔV s satisfying $|\Delta V| < 22$ m/s are used to adjust the transfer trajectory. This result implies that further investigation may be necessary to improve the design of transfer arcs between lobe sequences and circular orbits, which is left for future work.

The obtained results demonstrate that the proposed method can systematically incorporate multiple lobe dynamics into trajectory design by constructing a graph that represents possible transfer paths. This method combines chaotic orbits within effective lobes based on the targeting strategy. The Earth-Moon transfers are then realized by connecting trajectories within lobes to lunar transfer arcs through tubes.

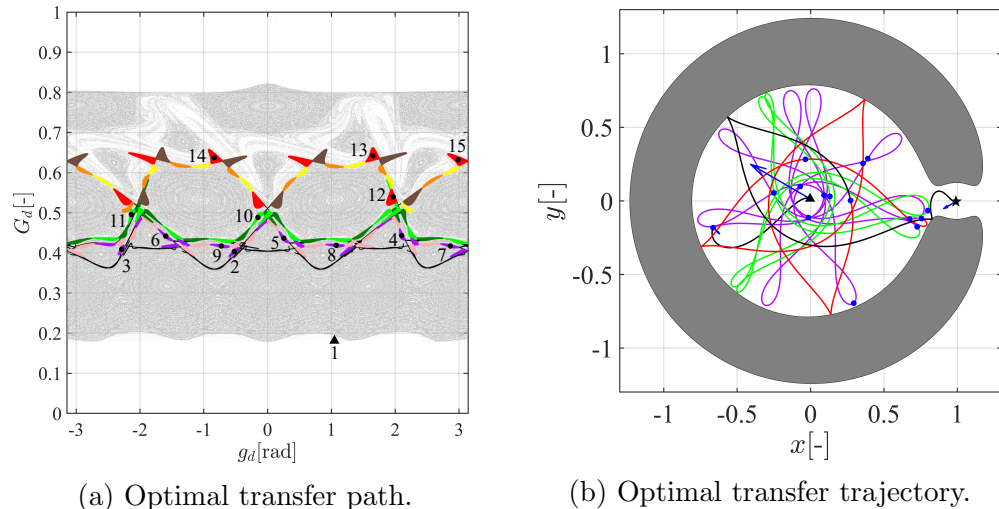


Figure 22: Optimal solution for the Earth–Moon transfer.

5.3. Role of lobe dynamics with respect to WSB

This subsection discusses the difference between the concept of lobe dynamics and extended WSB [79], both of which are related to resonance transitions. The optimal trajectory in Fig. 22(b) is a good example for investigating this difference. Figure 23 shows extended WSBs along this trajectory by yellow thick lines. Specifically, in Fig. 23(a), some transfer arcs within effective lobe sequences pass through extended WSBs, i.e., experience weak capture at the Moon. The time history of the semi-major axis along the optimal trajectory is shown in Fig. 23(b). The dashed lines indicate the values from Eq. (7) for the corresponding resonance ratios. The blue lines indicate impulsive ΔV s, and the other colored lines represent the transfer arcs within the lobe sequences of the corresponding colors.

Although the WSB is helpful for constructing ballistic lunar transfers, Fig. 23(b) demonstrates that weak capture does not always cause resonance transition. Thus, traversing extended WSBs may not be a sufficient condition to perform resonance transitions, as discussed in Ref. [79].

On the other hand, analyzing lobe dynamics in Fig. 9 aids in roughly predicting changes in resonance ratios, as shown in Fig. 23(b). Based on this analysis, the proposed method can efficiently connect lobe sequences to

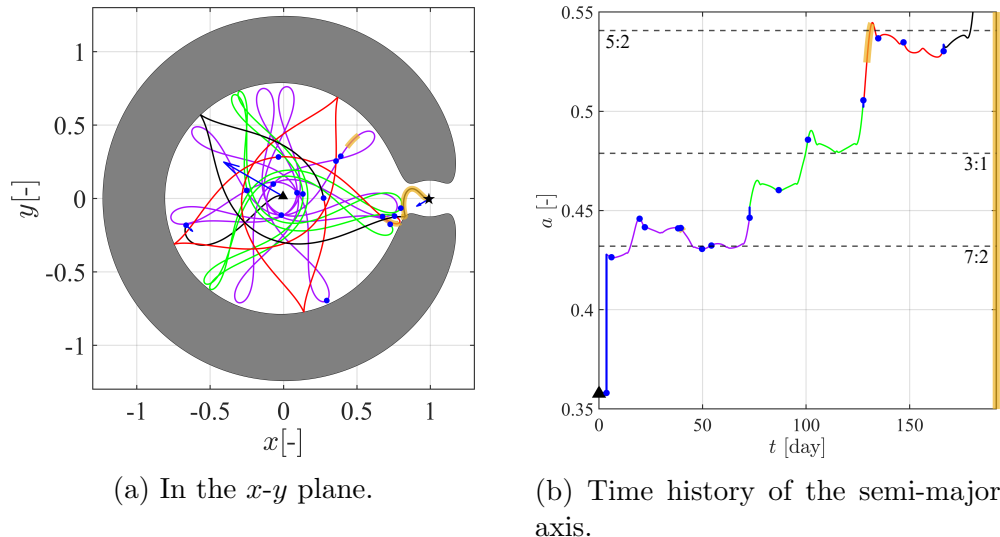


Figure 23: Optimal trajectory in Fig. 22(b) and its semi-major axis with extended WSB.

increase/decrease resonance ratios. Thus, lobe dynamics is advantageous for designing transfer trajectories.

6. Extension of the obtained results into the BCR4BP

In this section, the optimal trajectory obtained in Section 5 is extended to the BCR4BP to demonstrate the effectiveness of the proposed method [99]. Ballistic lunar transfers, such as the trajectory shown in Fig. 22(b), can be categorized into two types: exterior and interior. Exterior transfers are trajectories that arrive at the Moon from the Earth–Moon L_2 side and are often designed based on WSBs [87] or Poincaré maps [31, 40]. Interior transfers arrive at the Moon from the Earth–Moon L_1 side. This section focuses only on interior Earth–Moon transfers because the graph constructed in Section 5 does not include paths for exterior lunar transfers.

6.1. Optimization of the Earth–Moon transfer trajectory

The optimal Earth–Moon transfer in the BCR4BP is constructed simply by using the optimal trajectory in the CR3BP as an initial guess and solving a minimum-fuel optimization problem with the multiple-shooting scheme. As illustrated in Fig. 24, the initial guess is constructed by propagating the centroids of effective lobes forward and backward in time. Every transfer arc is then subdivided into shorter segments to ensure that the transfer time of each segment is approximately $\Delta t \simeq 1$. In this case, the total number of segments is determined to be $N = 45$. The initial points of each segment are propagated using Eq. (19) in the optimization. As the BCR4BP is a non-autonomous but periodic system, the initial phase angle of the Sun, θ_s^* , is set

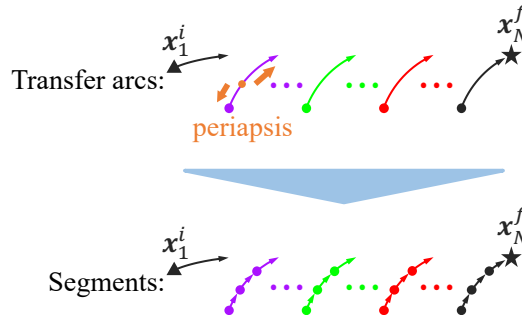


Figure 24: Illustration of the segments to construct the initial guess.

as $\theta_s^* = k\pi/6$ ($k = 0, 1, \dots, 11$). Thus, 12 initial guesses, the same trajectory segments with different values of θ_s^* , are used. To obtain the minimum-fuel interior Earth–Moon transfer in the BCR4BP, the optimization problem is formulated as follows:

$$\text{minimize} \quad |\Delta \mathbf{V}_E| + \sum_{n=1}^{N-1} |\mathbf{v}_{n+1}^i - \mathbf{v}_n^f| + |\Delta \mathbf{V}_M| \quad (25)$$

$$\text{subject to} \quad \mathbf{r}_1^i = \mathbf{r}_E \quad (26)$$

$$\theta_{s,1}^i = \theta_s^* \quad (27)$$

$$\mathbf{r}_{n+1}^i = \mathbf{r}_n^f \quad (n = 1, 2, \dots, N-1) \quad (28)$$

$$\theta_{s,n+1}^i = \theta_{s,n}^f \quad (n = 1, 2, \dots, N-1) \quad (29)$$

$$\mathbf{r}_N^f = \mathbf{r}_M \quad (30)$$

where the position, velocity, and phase angle of the Sun along the n -th segment are denoted by \mathbf{r}_n , \mathbf{v}_n , and $\theta_{s,n}$, respectively ($n = 1, 2, \dots, N$). The starting position at the LEO is expressed as \mathbf{r}_E , while the final position at the LLO is expressed as \mathbf{r}_M . These positions \mathbf{r}_E and \mathbf{r}_M are the same as those in the optimal trajectory in Fig. 22(b). The initial and final values of each segment are expressed by $(\cdot)^i$ and $(\cdot)^f$, respectively. In this problem, $\Delta \mathbf{V}_E$ and $\Delta \mathbf{V}_M$ can be applied along any direction. The optimization problem is solved using the *fmincon* function in MATLAB with the SQP algorithm.

The obtained results are summarized in Table 2. This table uses a “-” to denote that the optimization with the corresponding θ_s^* does not converge after 50000 iterations. All the converged solutions have a transfer time similar to that of the initial guess (191.8994 days), but the total ΔV varies significantly. The best solution in this table is the one with $\theta_s^* = 0$. Figure 25 illustrates the optimal trajectory in the BCR4BP with $\theta_s^* = 0$. The dashed line in this figure represents the optimal trajectory in the CR3BP (Fig. 22(b)), while the solid line indicates the optimal trajectory in the BCR4BP. The triangle and star in this figure correspond to the start and goal points, respectively. Similar to Fig. 22(b), blue arrows indicate $\Delta \mathbf{V}$ vectors, and the length of these arrows corresponds to the relative magnitude of the $\Delta \mathbf{V}$ s. Unlike the optimal transfer in the CR3BP, the majority of the total ΔV is contributed solely by the two largest $\Delta \mathbf{V}$ s. Specifically, $|\Delta \mathbf{V}_E| = 3120.8662$ m/s is applied to depart the LEO, and $|\Delta \mathbf{V}_M| = 638.5176$ m/s is applied to arrive at the LLO. The other small $\Delta \mathbf{V}$ s satisfying $|\Delta \mathbf{V}| < 21$ m/s are used to adjust the transfer trajectory.

Table 2: Results of the optimization in the BCR4BP

θ_s^*	Total ΔV [m/s]	Transfer time [day]
0	3832.6088	193.2512
$\pi/6$	-	-
$\pi/3$	-	-
$\pi/2$	5201.0019	191.7576
$2\pi/3$	3841.6832	193.7585
$5\pi/6$	-	-
π	-	-
$7\pi/6$	-	-
$4\pi/3$	-	-
$3\pi/2$	4934.6452	192.5052
$5\pi/3$	3848.4479	193.9369
$11\pi/6$	3837.8299	193.3733

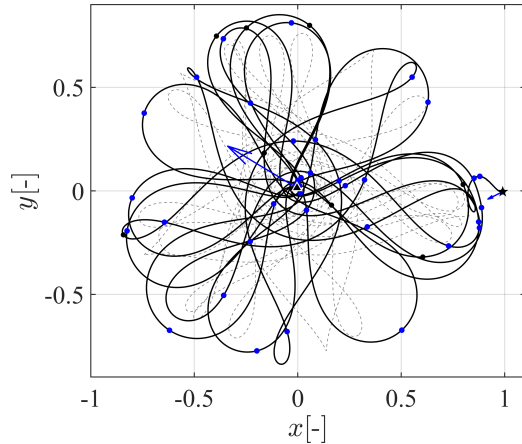


Figure 25: Optimal interior Earth–Moon transfer in the BCR4BP.

6.2. Comparison of the obtained results with literature

The results obtained in the BCR4BP are compared with those of the previous studies [22, 100–107]. The known results of impulsive interior transfers from the LEO with an altitude of 167 km to the LLO with an altitude of 100 km are summarized in Table 3 based on Topputto [22]. The previous studies have employed various dynamical models for the transfer design, making direct comparisons difficult. However, the results in the literature

Table 3: List of known Earth–Moon interior transfers between the LEO with an altitude of 167 km and the LLO with an altitude of 100 km.

References	Total ΔV [m/s]	Transfer time [day]
Hohmann transfer [22]	3954	5
Sweetser [100]	3726	-
Pernicka <i>et al.</i> [101]	3824	292
Yagasaki [102]	3925	31
	3947	14
	3951	4
Yagasaki [103]	3941	14
	3949	5
Topputo <i>et al.</i> [104]	3895	256
	3900	194
Mengali and Quarta [105]	3861	85
	3920	68
	3950	14
	4005	3
Mingotti <i>et al.</i> [106]	3896	31
	3917	30
	3936	14
Da Silva Fernandes and Marinho [107]	3850	58
	3902	32
	3943	14
	3950	5
Topputo [22]	3893	31
	3937	14
	3945	5

are valuable for estimating Pareto-optimal solutions for this transfer problem. Specifically, Sweetser [100] estimated the theoretical minimum total ΔV (3726 m/s) for the transfer between the given LEO and LLO. Topputo [22] calculated the Hohmann transfer between the LEO and LLO, with a total ΔV of 3954 m/s and transfer time of 5 days.

The result of the comparison is summarized in Fig. 26. This figure illustrates that the proposed method can identify one of the Pareto-optimal solutions with a medium transfer time. The obtained transfer with $\theta_s^* = 0$ may be helpful, especially for missions with strict fuel constraints, such as CubeSat missions. Note that it may be possible to find better solutions by adjusting the initial LEO point, the final LLO point, and the initial phase angle of the Sun.

6.3. Analysis of the optimal Earth–Moon transfer

To investigate transfer structures in the BCR4BP, this subsection analyzes the optimal trajectory in the BCR4BP with $\theta_s^* = 0$. Although analyzing dynamical structures in the higher-dimensional system of the BCR4BP is challenging, a numerical investigation is conducted along the optimal trajectory.

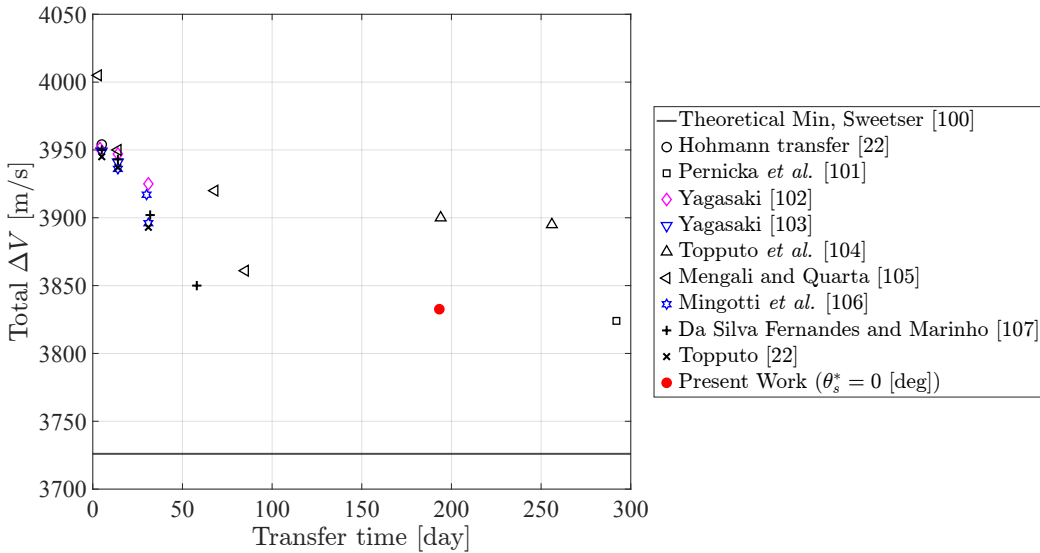


Figure 26: Comparison of impulsive interior Earth–Moon transfers with respect to the total ΔV and transfer time.

First, the existence of lobe dynamics in the BCR4BP is numerically investigated based on mean-motion resonances. The time history of the semi-major axis along the optimal trajectory in the BCR4BP is shown in Fig. 27. The dashed lines in Fig. 27 indicate the values from Eq. (7) for the corresponding resonance ratios, and the blue lines indicate impulsive $\Delta\mathbf{V}$ s. Note that Fig. 27(a) is the same as Fig. 23(b). Similar to Fig. 27(a), some parts of the semi-major axis in Fig. 27(b) are roughly constant. This result suggests that mean-motion resonances may also be important for transfers in the BCR4BP; therefore, the analysis of lobe dynamics in the BCR4BP is a promising direction for future work. Interestingly, small impulsive maneuvers with $\Delta V < 21$ m/s can significantly alter the semi-major axis.

Next, the existence of tube dynamics in the BCR4BP is examined along the optimal trajectory. Figure 28 indicates the Jacobi constant in the Earth–Moon CR3BP along the optimal trajectory in Fig. 25, perturbed by the gravitational force of the Sun. The red dashed lines show the reference in the CR3BP with $C_J = 3.16$, and the blue lines indicate impulsive $\Delta\mathbf{V}$ s. The cyan thick line in Fig. 28(a) shows the perturbed Jacobi constant $C_J \simeq 3.16$ (precisely, $3.1551 < C_J < 3.1666$), and the corresponding optimal trajectory is also plotted as the cyan thick line in Fig. 28(b). This result implies that the transfer structure to the Moon in the CR3BP with $C_J = 3.16$, i.e., the stable manifold of the L_1 Lyapunov orbit in Fig. 14, may remain in the BCR4BP.

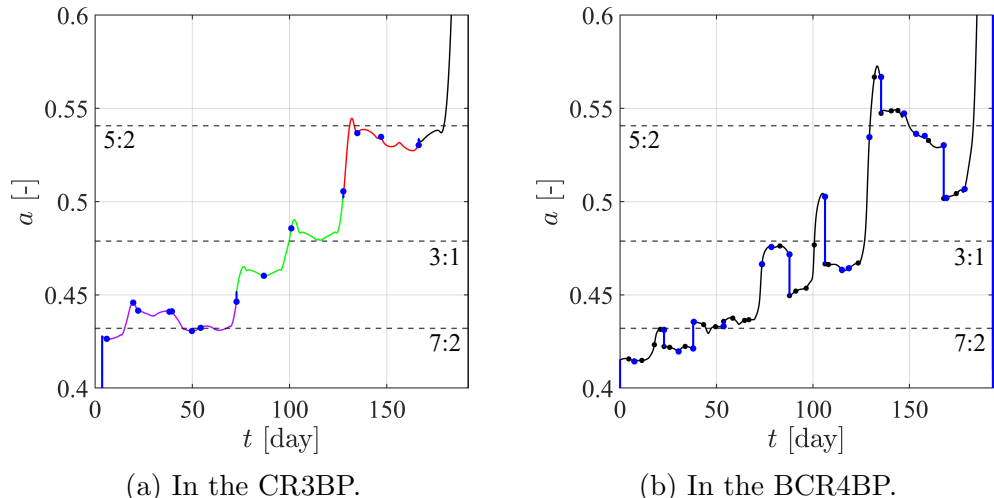
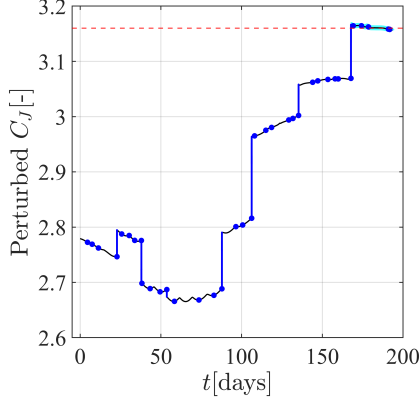
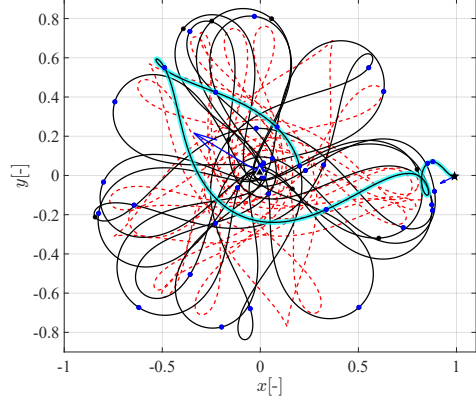


Figure 27: Time history of the semi-major axis along the optimal trajectory.



(a) Jacobi constant.



(b) Optimal trajectory in Fig. 25.

Figure 28: Jacobi constant in the Earth–Moon CR3BP along the optimal trajectory in Fig. 25.

For the analysis of transfer structures in Fig. 28, Lagrangian coherent structures (LCSs) [108–110] are leveraged. Haller [109] has defined LCSs as local extrema of the finite-time Lyapunov exponent (FTLE). The FTLE at \mathbf{x} from $t = 0$ to $t = T$ is defined as

$$\sigma(\mathbf{x}, T) = \frac{1}{|T|} \ln \|\Phi(T, 0)\| \quad (31)$$

where $\Phi(T, 0)$ is the state transition matrix from $t = 0$ to $t = T$ along the reference trajectory starting from \mathbf{x} , and $\|\Phi(T, 0)\|$ denotes the square root of the largest eigenvalue of the Cauchy–Green strain tensor $\Phi(T, 0)^T \Phi(T, 0)$. In autonomous systems, LCSs correspond to the stable and unstable manifolds associated with periodic orbits; in non-autonomous systems, LCSs can represent manifold-like lines or surfaces that mediate phase space transport. Previous studies have demonstrated that LCSs can be detected based on the FTLE in the CR3BP [111, 112] and in the elliptic restricted three-body problem [113]. Reference [114] has investigated LCSs in the CR3BP, BCR4BP, and the Sun–Earth–Moon ephemeris model by analyzing the FTLE fields.

Similar to Ref. [114], the FTLE field on the surface of section at $x = 0.8$ is examined under the dynamics of the BCR4BP. For the calculation of FTLE fields, a grid of 1000×1000 points is set within the region of $-0.1658 \leq y \leq 0.1658$ and $-0.2325 \leq \dot{y} \leq 0.2325$. The forward-time FTLE fields in the CR3BP and BCR4BP (with $\theta_s^* = 297.1825$ deg) are calculated with

$T = 14$ days, as shown in Fig. 29. In Fig. 29(a), the dotted line denotes the stable manifold of the L_1 Lyapunov orbit in Fig. 14 at $x = 0.8$. It is confirmed that the ridges in the FTLE field in the CR3BP match this stable manifold for this time interval. Figure 29(b) shows the FTLE field in the BCR4BP. The cross represents the optimal trajectory in Fig. 25 at $x = 0.8$, and thus this trajectory is located slightly inside of the ridges of the FTLE field in the BCR4BP. Note that the phase angle of the Sun is $\theta_s = 297.1825$ deg at this point. This result reveals that the optimal trajectory passes through the region divided by the LCS in the BCR4BP for the transfer to the Moon, and this LCS in the BCR4BP can be understood as the perturbed stable manifold of the L_1 Lyapunov orbit with $C_J = 3.16$ in the CR3BP.

7. Conclusions and future work

This paper proposes and validates a new method for systematically designing low-energy transfers by combining multiple lobe dynamics for space-craft trajectory design. The numerical difficulty of detecting lobe sequences, i.e., transport structures by lobe dynamics, is avoided by focusing on effective lobes. The concept of effective lobes is also valuable for trajectory design, as its definition implies that the designed trajectory is robust to small errors. Effective lobes are utilized as intermediate transfer points between start and goal orbits. The combination of effective lobe sequences is determined by exploiting a weighted, directed graph that represents possible transfer paths.

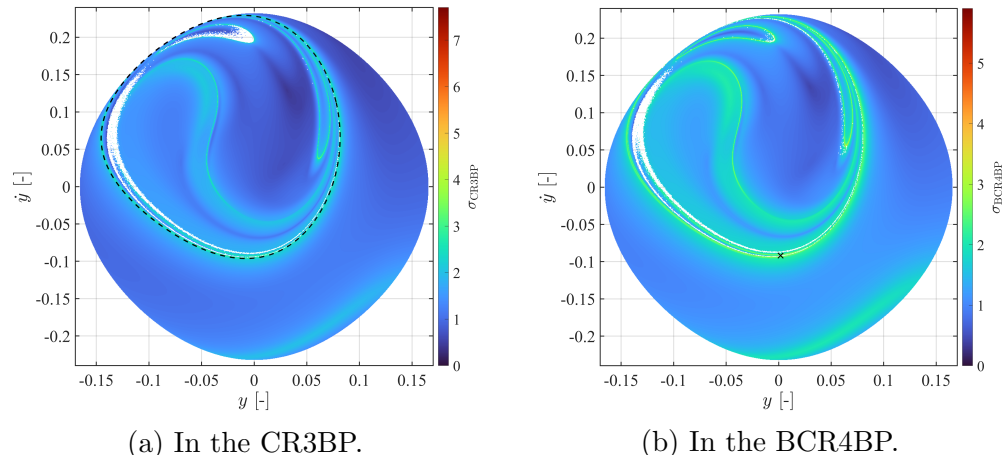


Figure 29: Forward-time FTLE fields at $x = 0.8$ in the CR3BP and BCR4BP.

In the graph, the transfer arcs between each point are determined by the targeting strategy. This graph aids in solving the combinatorial optimization to find the desired transfers. Thus, the proposed method constructs low-energy transfers by connecting chaotic orbits via effective lobes and offers a new type of transfer option.

The numerical results in Sections 4 and 5 demonstrate a way to combine lobe and tube dynamics. In other words, lobe dynamics can be utilized to identify transport structures between a celestial body and tubes of libration point orbits. Thus, the proposed framework advances the geometrical approach to trajectory design.

This paper also illustrates the application of the proposed method to the design of fuel-optimal transfers from a low Earth orbit to a low lunar orbit. In Section 6, the optimization of the Earth–Moon transfer trajectory in the BCR4BP enables comparison of the fuel consumption and transfer time with previous studies [22, 100–107]. The effectiveness of the proposed method is verified by demonstrating that it can help identify one of the Pareto-optimal solutions. Note that the proposed framework can easily be applied to other transfer problems by replacing the start and goal points with preferred ones.

A natural progression of this study is to extend the proposed method by leveraging lobe dynamics in a higher-dimensional phase space, such as the spatial CR3BP or the BCR4BP. It is necessary to develop a method to understand the higher-dimensional phase space using at most three-dimensional figures for trajectory design. Another direction of future work is to verify some aspects of the proposed method. The robustness of transfer trajectories designed by the proposed method can be explored in mission scenarios with small uncertainties. It is also essential to improve the method for determining transfer arcs, especially for connecting trajectories with different Jacobi constants.

Acknowledgments

The first author thanks the support of Japan Society for the Promotion of Science (JSPS) KAKENHI Grant No. JP 23KJ1692. The third author was supported by JSPS Grant-in-Aid for Scientific Research (B), JP No. 21H01002.

Declaration of Generative AI and AI-assisted technologies in the writing process

During the preparation of this work, the authors used Grammarly and ChatGPT 4.1 in order to improve readability. After using this tool, the authors reviewed and edited the content as needed and take full responsibility for the content of the publication.

References

- [1] S. Creech, J. Guidi, D. Elburn, Artemis: An Overview of NASA's Activities to Return Humans to the Moon, in: 2022 IEEE Aerospace Conference (AERO), Big Sky, MT, USA, 2022. doi:10.1109/AERO53065.2022.9843277.
- [2] J. R. Kopacz, R. Herschitz, J. Roney, Small satellites an overview and assessment, *Acta Astronaut.* 170 (2020) 93–105. doi:10.1016/j.actaastro.2020.01.034.
- [3] E. Turan, S. Speretta, E. Gill, Autonomous navigation for deep space small satellites: Scientific and technological advances, *Acta Astronaut.* 193 (2022) 56–74. doi:10.1016/j.actaastro.2021.12.030.
- [4] L. Liu, J. feng Cao, Y. Liu, S. jie Hu, G. shi Tang, J. feng Xie, CHANG'E-3 contingency scheme and trajectory, *Adv. Space Res.* 55 (2015) 1074–1084. doi:10.1016/j.asr.2014.11.025.
- [5] W. Zuo, C. Li, Z. Zhang, X. Zeng, Y. Liu, Y. Xiong, China's Lunar and Planetary Data System: Preserve and Present Reliable Chang'e Project and Tianwen-1 Scientific Data Sets, *Space Sci. Rev.* 217 (2021) 88. doi:10.1007/s11214-021-00862-3.
- [6] A. L. Batcha, J. Williams, T. F. Dawn, J. P. Gutkowski, M. V. Widner, S. L. Smallwood, B. J. Killeen, E. C. Williams, R. E. Harpold, Artemis I trajectory design and optimization, in: 2020 AAS/AIAA Astrodynamics Specialist Conference, Virtual, 2020.
- [7] R. A. Eckman, C. Barrett, A. L. Batcha, B. J. Killeen, Trajectory Operations of the Artemis I Mission, in: 2023 AAS/AIAA Astrodynamics Specialist Conference, Big Sky, MT, USA, 2023.

- [8] S. Mathavaraj, K. Negi, Chandrayaan-3 Trajectory Design: Injection to Successful Landing, *J. Spacecr. Rockets* (2024). doi:10.2514/1.A35980.
- [9] K. Uesugi, H. Matsuo, J. Kawaguchi, T. Hayashi, Japanese first double lunar swingby mission “Hiten”, *Acta Astronaut.* 25 (7) (1991) 347–355. doi:10.1016/0094-5765(91)90014-V.
- [10] K. Uesugi, Results of the MUSES-A “HITEN” mission, *Adv. Space Res.* 18 (1996) 69–72. doi:10.1016/0273-1177(96)00090-7.
- [11] G. D. Racca, A. Marini, L. Stagnaro, J. van Dooren, L. di Napoli, B. H. Foing, R. Lumb, J. Volp, J. Brinkmann, R. Grünagel, D. Estublier, E. Tremolizzo, M. McKay, O. Camino, J. Schoemaekers, M. Hechler, M. Khan, P. Rathsman, G. Andersson, K. Anflo, S. Berge, P. Bodin, A. Edfors, A. Hussain, J. Kugelberg, N. Larsson, B. Ljung, L. Meijer, A. Mörtsell, T. Nordebäck, S. Persson, F. Sjöberg, SMART-1 mission description and development status, *Planet. Space Sci.* 50 (2002) 1323–1337. doi:10.1016/S0032-0633(02)00123-X.
- [12] B. Foing, G. Racca, A. Marini, D. Koschny, D. Frew, B. Grieger, O. Camino-Ramos, J. Josset, M. Grande, SMART-1 technology, scientific results and heritage for future space missions, *Planet. Space Sci.* 151 (2018) 141–148. doi:10.1016/j.pss.2017.09.002.
- [13] M. T. Zuber, D. E. Smith, D. H. Lehman, T. L. Hoffman, S. W. Asmar, M. M. Watkins, Gravity Recovery and Interior Laboratory (GRAIL): Mapping the Lunar Interior from Crust to Core, *Space Sci. Rev.* 178 (2013) 3–24. doi:10.1007/s11214-012-9952-7.
- [14] T. Gardner, B. Cheetham, J. S. Parker, A. Forsman, E. Kayser, M. Thompson, C. Ott, L. DeMoudt, M. Caudill, M. Bolliger, A. Kam, K. Thompson, R. Rogers, H. Umansky, B. Bryant, T. Svitek, CAP-STONE: Mission Updates and Ongoing Efforts at the Moon, in: *ASCEND 2023*, Las Vegas, NV, USA, 2023. doi:10.2514/6.2023-4611.
- [15] T. Ishida, S. Fukuda, K. Kariya, H. Kamata, K. Takadama, H. Kojima, S. Sawai, S. Sakai, Vision-based navigation and obstacle detection flight results in SLIM lunar landing, *Acta Astronaut.* 226 (2025) 772–781. doi:10.1016/j.actaastro.2024.11.002.

- [16] K. Kitamura, Y. Shibasaki, Y. Ogura, Y. Sugimoto, S. Ueda, S. Sawai, S. Sakai, Trajectory Design and Flight Results of SLIM mission, in: 35th AAS/AIAA Space Flight Mechanics Meeting, Kaua'i, Hawaii, USA, 2025.
- [17] S. Ueda, T. Ito, K. Yokota, S. ichiro Sakai, T. Ishida, Y. Miyazawa, K. Kushiki, S. Fukuda, S. Sawai, On-orbit operation results of the powered descent guidance algorithm for pinpoint lunar landing, *Acta Astronaut.* 236 (2025) 47–61. doi:10.1016/j.actaastro.2025.06.039.
- [18] K. C. Howell, D. C. Davis, A. F. Haapala, Application of Peri-apse Maps for the Design of Trajectories Near the Smaller Primary in Multi-Body Regimes, *Math. Probl. Eng.* 2012 (2012) 351759. doi:10.1155/2012/351759.
- [19] M. Yamaguti, Towards the Harnessing of Chaos, Elsevier, Amsterdam, 1994.
- [20] H. Jaeger, H. Haas, Harnessing Nonlinearity: Predicting Chaotic Systems and Saving Energy in Wireless Communication, *Science* 304 (5667) (2004) 78–80. doi:10.1126/science.1091277.
- [21] R. P. Russell, Primer Vector Theory Applied to Global Low-Thrust Trade Studies, *J. Guid. Contr. Dyn.* 30 (2) (2007) 460–472. doi:10.2514/1.22984.
- [22] F. Toppato, On optimal two-impulse Earth–Moon transfers in a four-body model, *Celest. Mech. Astr.* 117 (2013) 279–313. doi:10.1007/s10569-013-9513-8.
- [23] K. Oshima, S. Campagnola, T. Yanao, Global search for low-thrust transfers to the Moon in the planar circular restricted three-body problem, *Celest. Mech. Dyn. Astr.* 128 (2017) 303–322. doi:10.1007/s10569-016-9748-2.
- [24] G. Grossi, C. Buonagura, C. Giordano, F. Toppato, On optimal three-impulse Earth–Moon transfers in a four-body model, *Celest. Mech. Dyn. Astr.* 136 (2024) 22. doi:10.1007/s10569-024-10193-4.

- [25] W. S. Koon, M. W. Lo, J. E. Marsden, S. D. Ross, Heteroclinic connections between periodic orbits and resonance transitions in celestial mechanics, *Chaos* 10 (2000) 427–469. doi:10.1063/1.166509.
- [26] W. S. Koon, M. W. Lo, J. E. Marsden, S. D. Ross, *Contemporary Mathematics*, Vol. 292, American Mathematical Society, 2002, Ch. Constructing a Low Energy Transfer Between Jovian Moons, pp. 129–145.
- [27] G. Gómez, W. S. Koon, M. W. Lo, J. E. Marsden, J. Masdemont, S. D. Ross, Connecting orbits and invariant manifolds in the spatial restricted three-body problem, *Nonlinearity* 17 (5) (2004) 1571–1606. doi:10.1088/0951-7715/17/5/002.
- [28] B. P. McCarthy, K. C. Howell, Four-body cislunar quasi-periodic orbits and their application to ballistic lunar transfer design, *Adv. Space Res.* 71 (2023) 556–584. doi:10.1016/j.asr.2022.09.020.
- [29] D. B. Henry, D. J. Scheeres, Fully numerical computation of heteroclinic connection families in the spatial three-body problem, *Commun. Nonlinear Sci. Numer. Simul.* 130 (2024) 107780. doi:10.1016/j.cnsns.2023.107780.
- [30] N. Hiraiwa, M. Bando, I. Nisoli, Y. Sato, Designing robust trajectories by lobe dynamics in low-dimensional Hamiltonian systems, *Phys. Rev. Res.* 6 (2024) L022046. doi:10.1103/PhysRevResearch.6.L022046.
- [31] S. T. Scheuerle Jr., K. C. Howell, D. C. Davis, Energy-informed pathways: A fundamental approach to designing ballistic lunar transfers, *Adv. Space Res.* (2024). doi:10.1016/j.asr.2024.07.035.
- [32] M. W. Lo, B. G. Williams, W. E. Bollman, D. Han, Y. Hahn, J. L. Bell, E. A. Hirst, R. A. Corwin, P. E. Hong, K. C. Howell, B. Barden, R. Wilson, Genesis Mission Design, *J. Astronaut. Sci.* 49 (1) (2001) 169–184. doi:10.1007/BF03546342.
- [33] D. S. Burnett, A. J. G. Jurewicz, D. S. Woolum, The future of Genesis science, *Meteorit. Planet. Sci.* 54 (2019) 1092–1114. doi:10.1111/maps.13266.

- [34] W. S. Koon, J. E. Marsden, S. D. Ross, M. Lo, D. J. Scheeres, Geometric Mechanics and the Dynamics of Asteroid Pairs, *Ann. N.Y. Acad. Sci.* 1017 (2004) 11–38. doi:10.1196/annals.1311.002.
- [35] W. S. Koon, M. W. Lo, S. D. Ross, *Dynamical Systems, the Three-Body Problem and Space Mission Design*, Marsden Books, Online, 2022.
- [36] Y. Ren, J. J. Masdemont, G. Gómez, E. Fantino, Two mechanisms of natural transport in the Solar System, *Commun. Nonlinear Sci. Numer. Simul.* 17 (2012) 844–853. doi:10.1016/j.cnsns.2011.06.030.
- [37] V. Szebehely, *Theories of Orbits: The Restricted Problem of Three Bodies*, Academic Press, New York and London, 1967. doi:10.1016/B978-0-12-395732-0.X5001-6.
- [38] J. E. Marsden, S. D. Ross, New methods in celestial mechanics and mission design, *Bull. Amer. Math. Soc.* 43 (1) (2006) 43–73. doi:10.1090/S0273-0979-05-01085-2.
- [39] W. S. Koon, M. W. Lo, J. E. Marsden, S. D. Ross, Resonance and Capture of Jupiter Comets, *Celest. Mech. Dyn. Astr.* 81 (2001) 27–38. doi:10.1023/A:1013398801813.
- [40] W. S. Koon, M. W. Lo, J. E. Marsden, S. D. Ross, Low Energy Transfer to the Moon, *Celest. Mech. Dyn. Astr.* 81 (2001) 63–73. doi:10.1023/A:1013359120468.
- [41] G. Mingotti, F. Topputo, Earth–Mars transfers with ballistic escape and low-thrust capture, *Celest. Mech. Dyn. Astr.* 110 (2011) 169–188. doi:10.1007/s10569-011-9343-5.
- [42] V. Rom-Kedar, A. Leonard, S. Wiggins, An analytical study of transport, mixing and chaos in an unsteady vortical flow, *J. Fluid Mech.* 214 (1990) 347–394. doi:10.1017/S0022112090000167.
- [43] V. Rom-Kedar, S. Wiggins, Transport in Two-Dimensional Maps, *Arch. Ration. Mech. Anal.* 109 (1990) 239–298. doi:10.1007/BF00375090.

- [44] J. D. Meiss, Symplectic maps, variational principles, and transport, *Rev. Mod. Phys.* 64 (1992) 795–848. doi:10.1103/RevModPhys.64.795.
- [45] J. D. Meiss, Thirty years of turnstiles and transport, *Chaos* 25 (2015) 097602. doi:10.1063/1.4915831.
- [46] R. Camassa, S. Wiggins, Chaotic advection in a Rayleigh-Bénard flow, *Phys. Rev. A* 43 (1991) 774–797. doi:10.1103/PhysRevA.43.774.
- [47] J. Duan, S. Wiggins, Lagrangian transport and chaos in the near wake of the flow around an obstacle: a numerical implementation of lobe dynamics, *Nonlin. Processes Geophys.* 4 (1997) 125–136. doi:10.5194/npg-4-125-1997.
- [48] N. Malhotra, S. Wiggins, Geometric Structures, Lobe Dynamics, and Lagrangian Transport in Flows with Aperiodic Time-Dependence, with Applications to Rossby Wave Flow, *J. Nonlinear Sci.* 8 (1998) 401–456. doi:10.1007/s003329900057.
- [49] M. Watanabe, H. Yoshimura, Experimental Investigation of Lagrangian Coherent Structures and Lobe Dynamics in Perturbed Rayleigh-Bénard Convection, in: *Proceedings of the ASME 2021 Fluids Engineering Division Summer Meeting*, 2021. doi:10.1115/FEDSM2021-64945.
- [50] M. F. M. Speetjens, Linear vs nonlinear transport during chaotic advection in fluid flows, *Chaos* 32 (2022) 093113. doi:10.1063/5.0087258.
- [51] S. Wiggins, The Dynamical Systems Approach to Lagrangian Transport in Oceanic Flows, *Annu. Rev. Fluid Mech.* 37 (2005) 295–328. doi:10.1146/annurev.fluid.37.061903.175815.
- [52] F. Raynal, S. Wiggins, Lobe dynamics in a kinematic model of a meandering jet. I. Geometry and statistics of transport and lobe dynamics with accelerated convergence, *Physica D* 223 (2006) 7–25. doi:10.1016/j.physd.2006.07.021.
- [53] P. C. du Toit, J. E. Marsden, Horseshoes in hurricanes, *J. Fixed Point Theory Appl.* 7 (2010) 351–384. doi:10.1007/s11784-010-0028-6.

- [54] K. Oshima, T. Yanao, Jumping mechanisms of Trojan asteroids in the planar restricted three- and four-body problems, *Celest. Mech. Dyn. Astr.* 122 (2015) 53–74. doi:10.1007/s10569-015-9609-4.
- [55] V. Krajňák, H. Waalkens, Phase space structures causing the reaction rate decrease in the collinear hydrogen exchange reaction, *J. Math. Chem.* 58 (2020) 292–339. doi:10.1007/s10910-019-01083-4.
- [56] M. Katsanikas, V. J. García-Garrido, M. Agaoglou, S. Wiggins, Phase space analysis of the dynamics on a potential energy surface with an entrance channel and two potential wells, *Phys. Rev. E* 102 (2020) 012215. doi:10.1103/PhysRevE.102.012215.
- [57] M. Dellnitz, O. Junge, W. S. Koon, F. Lekien, M. W. Lo, J. E. Marsden, K. Padberg, R. Preis, S. D. Ross, B. Thiere, Transport in dynamical astronomy and multibody problems, *Int. J. Bifurc. Chaos* 15 (3) (2005) 699–727. doi:10.1142/S0218127405012545.
- [58] S. Naik, F. Lekien, S. D. Ross, Computational method for phase space transport with applications to lobe dynamics and rate of escape, *Regul. Chaot. Dyn.* 22 (2017) 272–297. doi:10.1134/S1560354717030078.
- [59] S. D. Ross, W. S. Koon, M. W. Lo, J. E. Marsden, Application of Dynamical Systems Theory to a Very Low Energy Transfer, in: 14th AAS/AIAA Space Flight Mechanics Conference, Maui, HI, USA, 2004.
- [60] P. Grover, S. Ross, Designing Trajectories in a Planet-Moon Environment Using the Controlled Keplerian Map, *J. Guid. Contr. Dyn.* 32 (2) (2009) 437–444. doi:10.2514/1.38320.
- [61] S. Odashima, K. Oshima, T. Yanao, Design of Earth–Moon transfer trajectories using multiple resonance gravity assists and invariant manifold tubes, in: 60th Space Sciences and Technology Conference, Hakodate, Japan, 2016 (In Japanese).
- [62] S. Odashima, K. Oshima, T. Yanao, Design of Earth–Moon Transfer Trajectories Based on Dynamical Mechanisms of Resonant Gravity Assists, in: 61st Space Sciences and Technology Conference, Niigata, Japan, 2017 (In Japanese).

- [63] B. V. Chirikov, A Universal Instability of Many-Dimensional Oscillator Systems, *Phys. Rep.* 52 (1979) 263–379. doi:10.1016/0370-1573(79)90023-1.
- [64] S. Huang, Very Restricted Four-Body Problem, Tech. rep., NASA Goddard Space Flight Center (1960).
- [65] K. K. Boudad, Trajectory Design between Cislunar Space and Sun–Earth Libration Points in a Four-Body Model, Ph.D. thesis, Purdue University (2022).
- [66] E. J. Doedel, V. A. Romanov, R. C. Paffenroth, H. B. Keller, D. J. Dichmann, J. Galán-Vioque, A. Vanderbauwhede, Elemental Periodic Orbits Associated with the Libration Points in the Circular Restricted 3-Body Problem, *Int. J. Bifurc. Chaos* 17 (8) (2007) 2625–2677. doi:10.1142/S0218127407018671.
- [67] D. Qiao, J. Zheng, Y. Qi, Cislunar L4 and L5 axial orbits and their applications, *Acta Astronaut.* 222 (2024) 457–470. doi:10.1016/j.actaastro.2024.06.025.
- [68] C. Chen, X. Li, D. Qiao, Stable configuration design for libration point gravitational wave observatory, *Acta Astronaut.* 226 (2025) 248–261. doi:10.1016/j.actaastro.2024.10.008.
- [69] S. Pan, X. Hou, Review Article: Resonant Families of Periodic Orbits in the Restricted Three-body Problem, *Res. Astron. Astrophys.* 22 (7) (2022) 072002. doi:10.1088/1674-4527/ac6aaa.
- [70] A. Rawat, B. Kumar, A. J. Rosengren, S. D. Ross, Cislunar Mean-Motion Resonances: Definitions, Widths, and Comparisons with Resonant Satellites, *J. Guid. Contr. Dyn.*(Articles in Advance). doi:10.2514/1.G009336.
- [71] M. Vaquero, K. C. Howell, Design of transfer trajectories between resonant orbits in the Earth–Moon restricted problem, *Acta Astronaut.* 94 (2014) 302–317. doi:10.1016/j.actaastro.2013.05.006.
- [72] R. L. Anderson, S. Campagnola, G. Lantoine, Broad search for unstable resonant orbits in the planar circular restricted three-body problem,

Celest. Mech. Dyn. Astr. 124 (2016) 177–199. doi:10.1007/s10569-015-9659-7.

- [73] R. F. Arenstorf, Existence of periodic solutions passing near both masses of the restricted three-body problem, AIAA Journal 1 (1) (1963) 238–240. doi:10.2514/3.1516.
- [74] S. Bonasera, N. Bosanac, Computing Natural Transitions Between Tori Near Resonances in the Earth–Moon System, J. Guid. Contr. Dyn. 46 (3) (2023) 443–454. doi:10.2514/1.G006941.
- [75] R. L. Anderson, Tour Design Using Resonant-Orbit Invariant Manifolds in Patched Circular Restricted Three-Body Problems, J. Guid. Contr. Dyn. 44 (1) (2021) 106–119. doi:10.2514/1.G004999.
- [76] D. Canales, M. Gupta, B. Park, K. C. Howell, A transfer trajectory framework for the exploration of Phobos and Deimos leveraging resonant orbits, Acta Astronaut. 194 (2022) 263–276. doi:10.1016/j.actaastro.2022.02.001.
- [77] D. J. Dichmann, R. Lebois, J. P. Carrico, Dynamics of Orbits Near 3:1 Resonance in the Earth–Moon System, J. Astronaut. Sci. 60 (2013) 51–86. doi:10.1007/s40295-014-0009-x.
- [78] J. J. K. Parker, R. L. Lebois, S. Lutz, C. Nickel, K. Ferrant, A. Michaels, Transiting Exoplanet Survey Satellite (TESS) Flight Dynamics Commissioning Results and Experiences, in: 2018 AAS/AIAA Astrodynamics Specialist Conference, Snowbird, UT, USA, 2018.
- [79] E. Belbruno, F. Topputo, M. Gidea, Resonance transitions associated to weak capture in the restricted three-body problem, Adv. Space Res. 42 (2008) 1330–1351. doi:10.1016/j.asr.2008.01.018.
- [80] E. Belbruno, B. G. Marsden, Resonance Hopping in Comets, Astron. J. 113 (4) (1997) 1433–1444.
- [81] G. Lantoine, R. P. Russell, S. Campagnola, Optimization of low-energy resonant hopping transfers between planetary moons, Acta Astronaut. 68 (7) (2011) 1361–1378. doi:10.1016/j.actaastro.2010.09.021.

[82] S. D. Ross, W. S. Koon, M. W. Lo, J. E. Marsden, Design of a Multi-Moon Orbiter, in: 13th AAS/AIAA Space Flight Mechanics Conference, Ponce, Puerto Rico, 2003.

[83] S. D. Ross, D. J. Scheeres, Multiple Gravity Assists, Capture, and Escape in the Restricted Three-Body Problem, *SIAM J. Appl. Dyn. Syst.* 6 (3) (2007) 576–596. doi:10.1137/060663374.

[84] S. Campagnola, B. B. Buffington, A. E. Petropoulos, Jovian tour design for orbiter and lander missions to Europa, *Acta Astronaut.* 100 (2014) 68–81. doi:10.1016/j.actaastro.2014.02.005.

[85] S. Campagnola, B. B. Buffington, T. Lam, A. E. Petropoulos, E. Pellegrini, Tour Design Techniques for the Europa Clipper Mission, *J. Guid. Contr. Dyn.* 42 (12) (2019) 2615–2626. doi:10.2514/1.G004309.

[86] E. A. Belbruno, Lunar Capture Orbits, a Method of Constructing Earth Moon Trajectories and the Lunar Gas Mission, in: 19th AIAA/DGLR/JSASS International Electric Propulsion Conference, Colorado Springs, CO, USA, 1987.

[87] E. A. Belbruno, J. K. Miller, Sun-Perturbed Earth-to-Moon Transfers with Ballistic Capture, *J. Guid. Contr. Dyn.* 16 (4) (1993) 770–775. doi:10.2514/3.21079.

[88] B. F. Villac, D. J. Scheeres, Escaping Trajectories in the Hill Three-Body Problem and Applications, *J. Guid. Contr. Dyn.* 26 (2) (2003) 224–232. doi:10.2514/2.5062.

[89] K. Ikeda, N. Hiraiwa, M. Bando, S. Hokamoto, Design of Low-Energy Transfer Trajectories from Jupiter to Europa with Ballistic Transfer, *J. Evol. Space Act.* 1 (2023) 35. doi:10.57350/jesa.35.

[90] D. A. Vallado, Fundamentals of Astrodynamics and Applications, 4th Edition, Microcosm Press, Hawthorne, CA, 2013.

[91] R. S. Mackay, J. D. Meiss, I. C. Percival, Resonances in area-preserving maps, *Physica D* 27 (1987) 1–20. doi:10.1016/0167-2789(87)90002-9.

[92] R. S. Mackay, J. D. Meiss, I. C. Percival, Transport in Hamiltonian systems, *Physica D* 13 (1984) 55–81. doi:10.1016/0167-2789(84)90270-7.

- [93] K. C. Howell, Three-dimensional, periodic, ‘halo’ orbits, *Celest. Mech.* 32 (1984) 53–71. doi:10.1007/BF01358403.
- [94] G. A. Tsirogiannis, A graph based methodology for mission design, *Celest. Mech. Dyn. Astr.* 114 (2012) 353–363. doi:10.1007/s10569-012-9444-9.
- [95] E. Trumbauer, B. Villac, Heuristic Search-Based Framework for On-board Trajectory Redesign, *J. Guid. Contr. Dyn.* 37 (1) (2014) 164–175. doi:10.2514/1.61236.
- [96] T. R. Smith, N. Bosanac, Motion Primitive Approach to Spacecraft Trajectory Design in a Multi-body System, *J. Astronaut. Sci.* 70 (2023) 34. doi:10.1007/s40295-023-00395-7.
- [97] K. Oshima, A graph-based framework of low-energy transfer design, *Acta Astronaut.* 229 (2025) 644–661. doi:10.1016/j.actaastro.2025.01.050.
- [98] T. Shinbrot, E. Ott, C. Grebogi, J. A. Yorke, Using chaos to direct trajectories to targets, *Phys. Rev. Lett.* 65 (1990) 3215–3218. doi:10.1103/PhysRevLett.65.3215.
- [99] N. Hiraiwa, M. Bando, S. Hokamoto, Extending Earth–Moon Transfer Based on Lobe Dynamics into the Restricted Four-Body Problem, in: 35th AAS/AIAA Space Flight Mechanics Meeting, Kaua’i, Hawaii, USA, 2025.
- [100] T. H. Sweetser, An Estimate of the Global Minimum ΔV Needed for Earth–Moon Transfer, in: AAS/AIAA Space Flight Mechanics Meeting, Houston, TX, USA, 1991.
- [101] H. J. Pernicka, D. P. Scarberry, S. M. Marsh, T. H. Sweetser, A search for low Δv Earth–to–Moon trajectories, in: Astrodynamics Conference, Scottsdale, AZ, USA, 1994.
- [102] K. Yagasaki, Computation of low energy Earth–to–Moon transfers with moderate flight time, *Physica D* 197 (3) (2004) 313–331. doi:10.1016/j.physd.2004.07.005.

- [103] K. Yagasaki, Sun-perturbed Earth–to–Moon transfers with low energy and moderate flight time, *Celest. Mech. Astr.* 90 (2004) 197–212. doi:10.1007/s10569-004-0406-8.
- [104] F. Topputo, M. Vasile, F. Bernelli-Zazzera, Earth–to–Moon Low Energy Transfers Targeting L_1 Hyperbolic Transit Orbits, *Ann. N.Y. Acad. Sci.* 1065 (2005) 55–76. doi:10.1196/annals.1370.025.
- [105] G. Mengali, A. Quarta, Optimization of Biimpulsive Trajectories in the Earth–Moon Restricted Three-Body System, *J. Guid. Contr. Dyn.* 28 (2) (2005) 209–216. doi:10.2514/1.7702.
- [106] G. Mingotti, F. Topputo, Ways to the Moon: A Survey, in: 21th AAS/AIAA Space Flight Mechanics Meeting, New Orleans, LA, USA, 2011.
- [107] S. Da Silva Fernandes, C. M. P. Marinho, Sun Influence on Two-Impulsive Earth–to–Moon Transfers, in: 22nd International Symposium on Space Flight Dynamics, São José dos Campos, Brazil, 2011.
- [108] G. Haller, G. Yuan, Lagrangian coherent structures and mixing in two-dimensional turbulence, *Physica D* 147 (3) (2000) 352–370. doi:10.1016/S0167-2789(00)00142-1.
- [109] G. Haller, Distinguished material surfaces and coherent structures in three-dimensional fluid flows, *Physica D* 149 (4) (2001) 248–277. doi:10.1016/S0167-2789(00)00199-8.
- [110] G. Haller, Lagrangian Coherent Structures, *Annu. Rev. Fluid Mech.* 47 (2015) 137–162. doi:10.1146/annurev-fluid-010313-141322.
- [111] C. R. Short, K. C. Howell, X. M. Tricoche, Lagrangian coherent structures in the restricted three-body problem, in: 21st AAS/AIAA Space Flight Mechanics Meeting, New Orleans, LA, USA, 2011.
- [112] D. Pérez, G. Gómez, J. J. Masdemont, Detecting Invariant Manifolds Using Hyperbolic Lagrangian Coherent Structures, in: 1st IAA Conference on Dynamics and Control of Space Systems (DyCoSS), Porto, Portugal, 2012.

- [113] E. S. Gawlik, J. E. Marsden, P. C. Du Toit, S. Campagnola, Lagrangian coherent structures in the planar elliptic restricted three-body problem, *Celest. Mech. Astr.* 103 (2009) 227–249.
- [114] C. R. Short, K. C. Howell, Lagrangian coherent structures in various map representations for application to multi-body gravitational regimes, *Acta Astronaut.* 94 (2014) 592–607. doi:10.1016/j.actaastro.2013.08.020.